NASA TECHNICAL MEMORANDUM

NASA TM X-64974

(NASA-TM-X-64974) X-RAY REFLECTION AND SCATTER MEASUREMENTS ON SELECTED OPTICAL SAMPLES (NASA) 77 p HC $5. CSCL 20F

N76-16918

Unclas
G3/74 09993

X-RAY REFLECTION AND SCATTER MEASUREMENTS ON SELECTED OPTICAL SAMPLES

By Stanley A. Fields, John M. Reynolds and Robert L. Holland
Space Sciences Laboratory

November 1975

NASA

George C. Marshall Space Flight Center
Marshall Space Flight Center, Alabama

TECHNICAL REPORT STANDARD TITLE PAGE

1. REPORT NO. NASA TM X-64974	2. GOVERNMENT ACCESSION NO.	3. RECIPIENT'S CATALOG NO.
4. TITLE AND SUBTITLE X-Ray Reflection and Scatter Measurements on Selected Optical Samples		5. REPORT DATE November 1975
		6. PERFORMING ORGANIZATION CODE
7. AUTHOR(S) Stanley A. Fields, John M. Reynolds, and Robert L. Holland		8. PERFORMING ORGANIZATION REPORT #
9. PERFORMING ORGANIZATION NAME AND ADDRESS George C. Marshall Space Flight Center, Marshall Space Flight Center, Alabama 35812		10. WORK UNIT NO.
		11. CONTRACT OR GRANT NO.
12. SPONSORING AGENCY NAME AND ADDRESS National Aeronautics and Space Administration, Washington, D.C. 20546		13. TYPE OF REPORT & PERIOD COVERED Technical Memorandum
		14. SPONSORING AGENCY CODE

15. SUPPLEMENTARY NOTES

Prepared by Space Sciences Laboratory, Science and Engineering

16. ABSTRACT

The results from an experimental program to determine the reflection efficiency and scatter parameters of selected optical samples are presented. The measurements were made using 8.34Å X-rays at various angles of incidence. Selected samples were contaminated after being measured and then remeasured to determine the effects of contamination.

The instrumentation involved in taking the data, including the X-ray reflectometer and data processing equipment, is discussed in detail. The condition of the optical surfaces, the total reflection measurements, the scatter measurements, and the analysis are discussed.

17. KEY WORDS	18. DISTRIBUTION STATEMENT Unclassified — Unlimited Stanley A. Fields

19. SECURITY CLASSIF. (of this report)	20. SECURITY CLASSIF. (of this page)	21. NO. OF PAGES	22. PRICE
Unclassified	Unclassified	76	NTIS

TABLE OF CONTENTS

LIST OF ILLUSTRATIONS

LIST OF ILLUSTRATIONS (Continued)

LIST OF ILLUSTRATIONS (Continued)

LIST OF ILLUSTRATIONS (Continued)

LIST OF ILLUSTRATIONS (Concluded)

X-RAY REFLECTION AND SCATTER MEASUREMENTS ON SELECTED OPTICAL SAMPLES

I. INTRODUCTION

The measurements described in this report were made to allow correlation between the reflection efficiency and the scatter properties of a particular sample. The measurements were all made at a wavelength of 8.34Å. The x-ray reflectometer was operated in a vacuum system which was oil-free and therefore did not contaminate the surface of the sample being studied.

Many experimenters have reported the results of total reflectivity measurements at x-ray wavelengths of a large variety of reflecting surfaces. A smaller number have reported the results of studies of scatter characteristics at x-ray wavelengths. These papers are listed in a bibliography to this report.

This report contains the results of measurements made on clean fused silica optical samples with a surface finish of $\lambda/10$ and on 1000Å thick chromium surfaces deposited on the fused silica surfaces. The samples were contaminated under controlled conditions and remeasured to determine the effects of contamination on the total reflection and scatter characteristics. The reflection efficiency measurements are compared to theoretical data. The smoothing of the scatter data, which are presented with the intensity (y) as a function of beam width (x), was performed by conventional least squares theory.

II. DESCRIPTION OF INSTRUMENTATION

A. X-Ray Reflectometer

The vacuum x-ray reflectometer instrument is designed to allow precision measurements of x-rays reflected by optical samples [1]. The reflectometer shown in Figure 1 was used to make the measurements discussed in this report. The instrument consists of a vacuum chamber, a microfocus x-ray

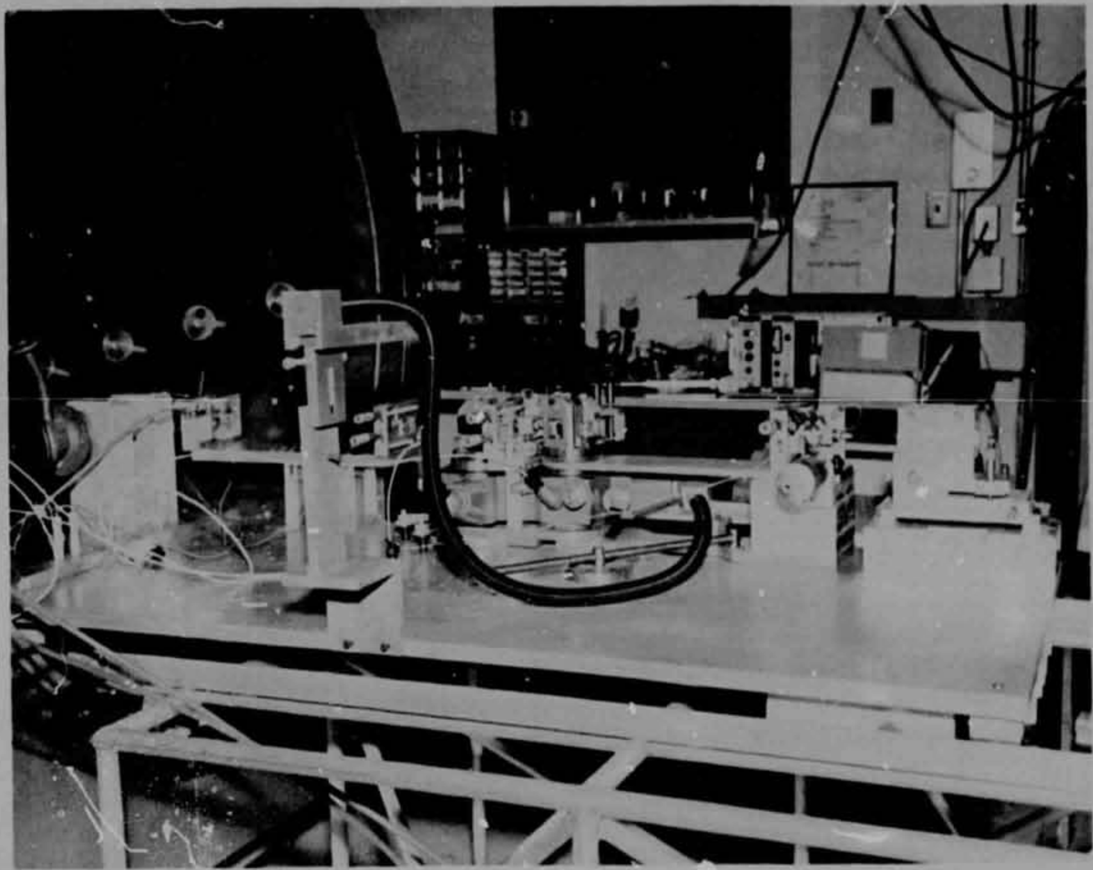

Figure 1. Vacuum x-ray reflectometer.

source, a filter for wavelength definition, a crystal monochromator for high wavelength resolution, a precision rotary table for positioning the optical sample, a detector for monitoring the x-ray beam prior to the optical sample, a detector for measuring the x-ray beam reflected by the optical sample, a series of slits to define the x-ray beam, and a remote readout system. The relative locations of the various elements and the slit dimensions used for the measurements to be discussed in this report are shown in Figure 2.

The environmental vacuum chamber (Fig. 3) which contains the x-ray reflectometer is completely oil-free and bakeable to 250°C when the reflectometer is removed. The chamber is 122 cm in diameter and 183 cm long. A small liquid nitrogen shroud 70 cm in diameter and 30 cm long is located in the rear of the chamber. The system is rough-pumped with four banks of

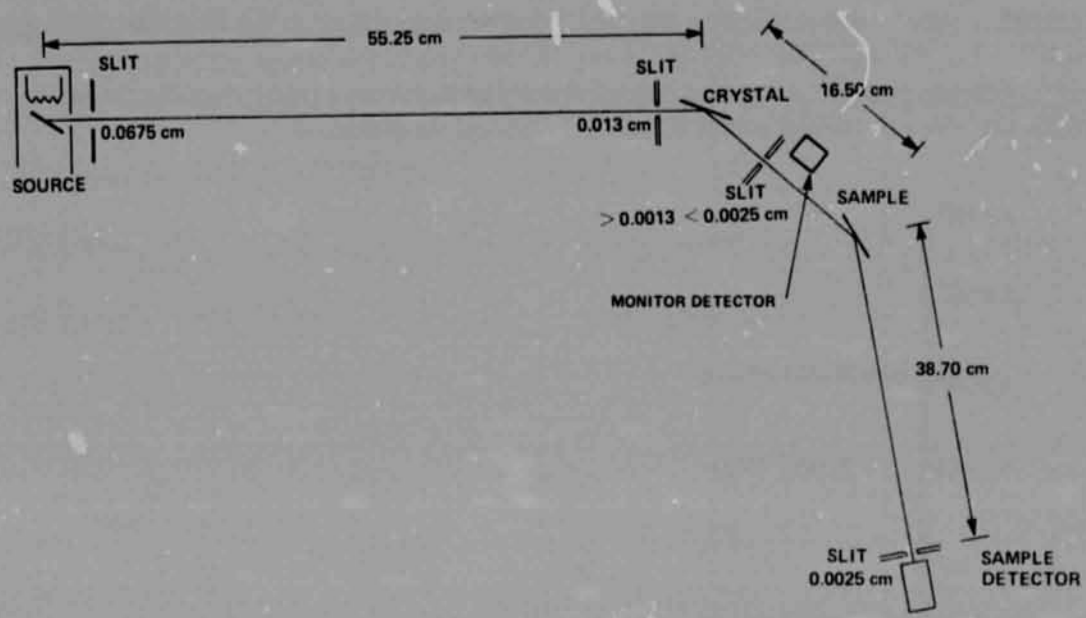

Figure 2. Schematic of x-ray reflectometer.

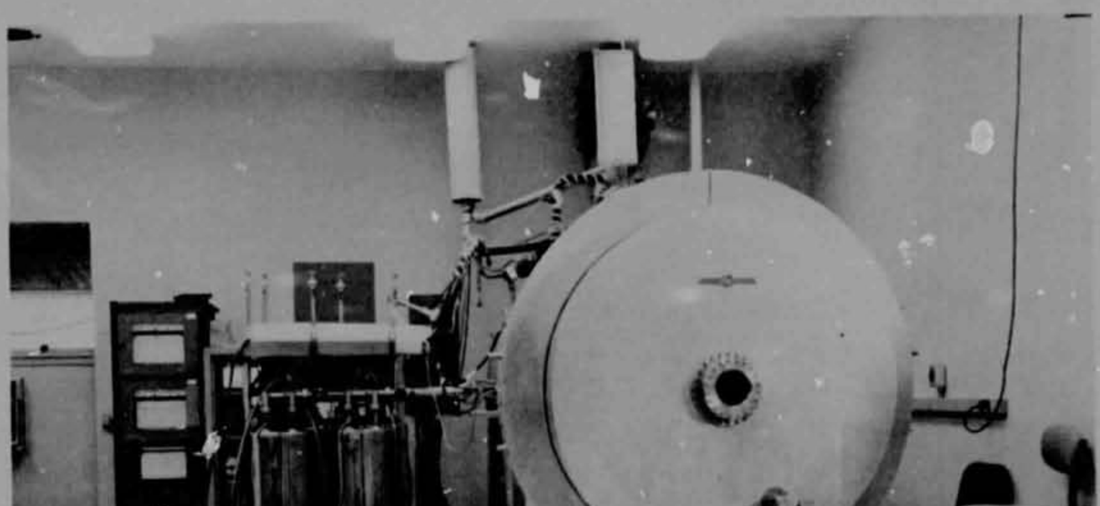

Figure 3. Environmental vacuum chamber.

sorption pumps mounted on a manifold that is connected to the chamber through a bakeable valve. The primary pump is a 3000 l/s ion pump and a secondary 1000 l/s ion pump. A typical pump-down curve for an empty chamber and one with the vacuum x-ray reflectometer is shown in Figure 4.

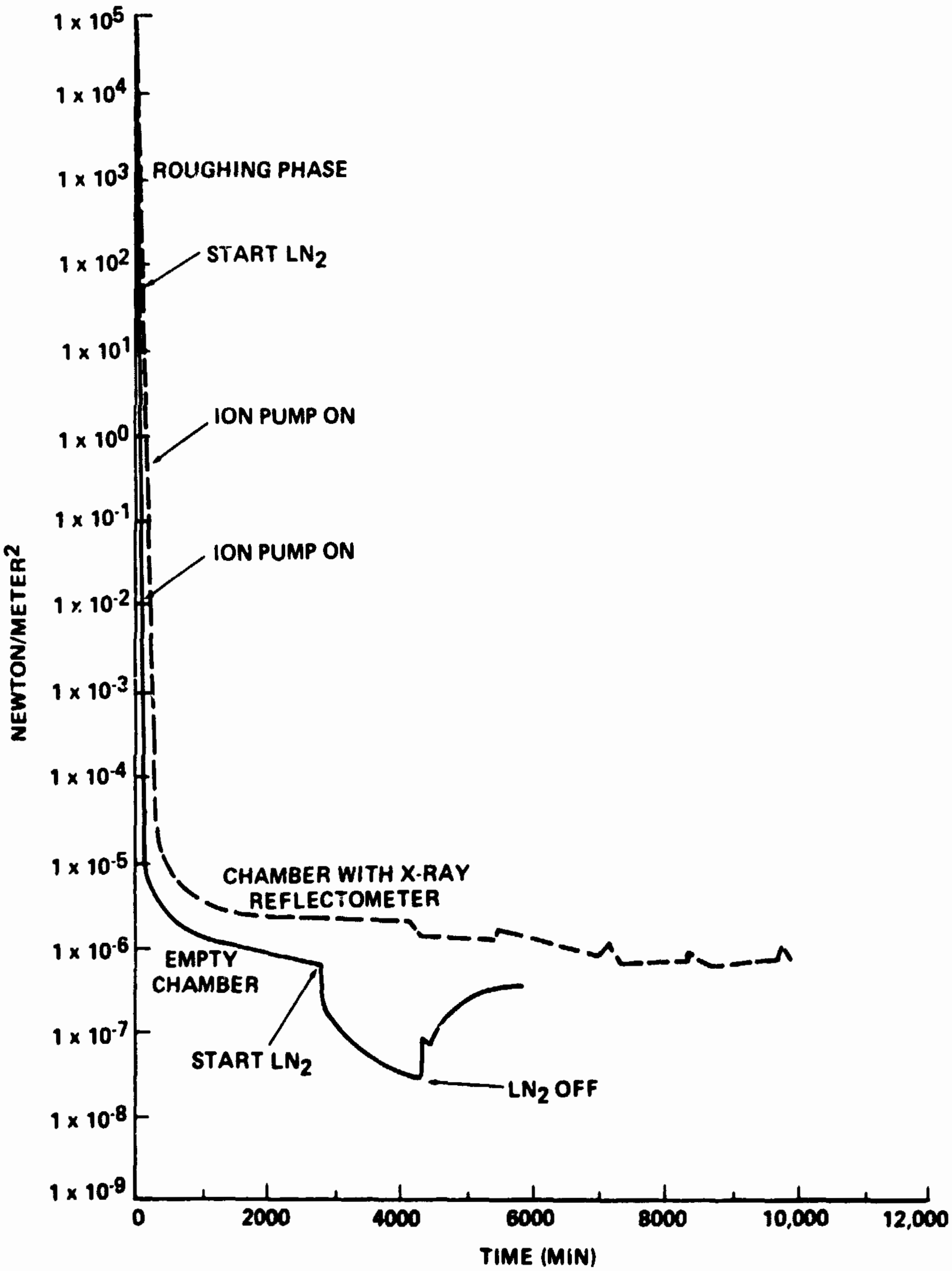

Figure 4. Environmental chamber pump-down curve.

The x-ray reflectometer is mounted on a baseplate 63 × 163 cm which can be removed from the vacuum chamber as required. The x-ray source is a microfocus, windowless x-ray tube. The dimensions of the emitting region of the x-ray source are approximately 0.2 × 4 mm, with the 4 mm dimension extended perpendicularly to the baseplate in Figure 5. The x-ray source was operated at 2400 V and 3.5 mA with an aluminum anode while taking the data discussed in this report.

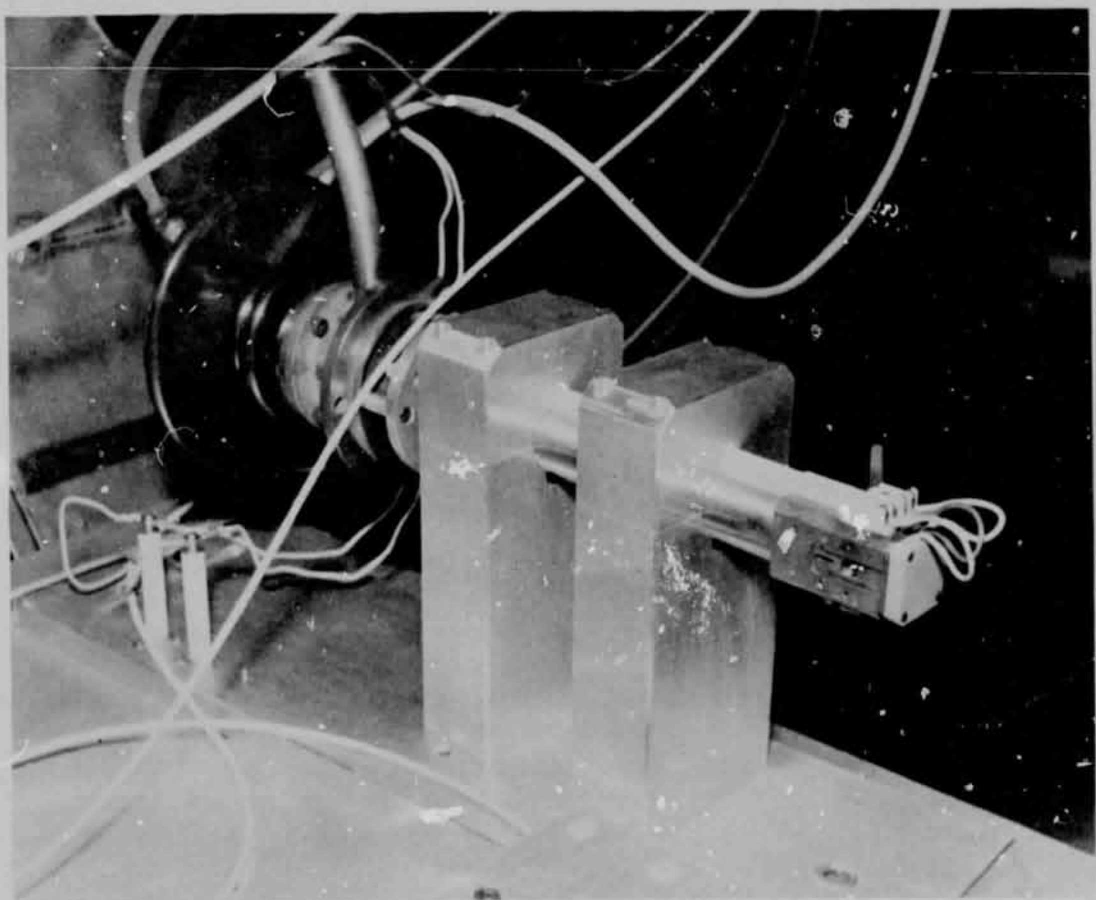

Figure 5. Microfocus x-ray tube.

A drawing of the sample holder is shown in Figure 6. The holder will accept four 2.54 cm diameter samples which are retained in the cylindrical wells on the four faces of the sample drum. The samples are spring-loaded from behind and are held in their wells by the retaining fingers. The sample

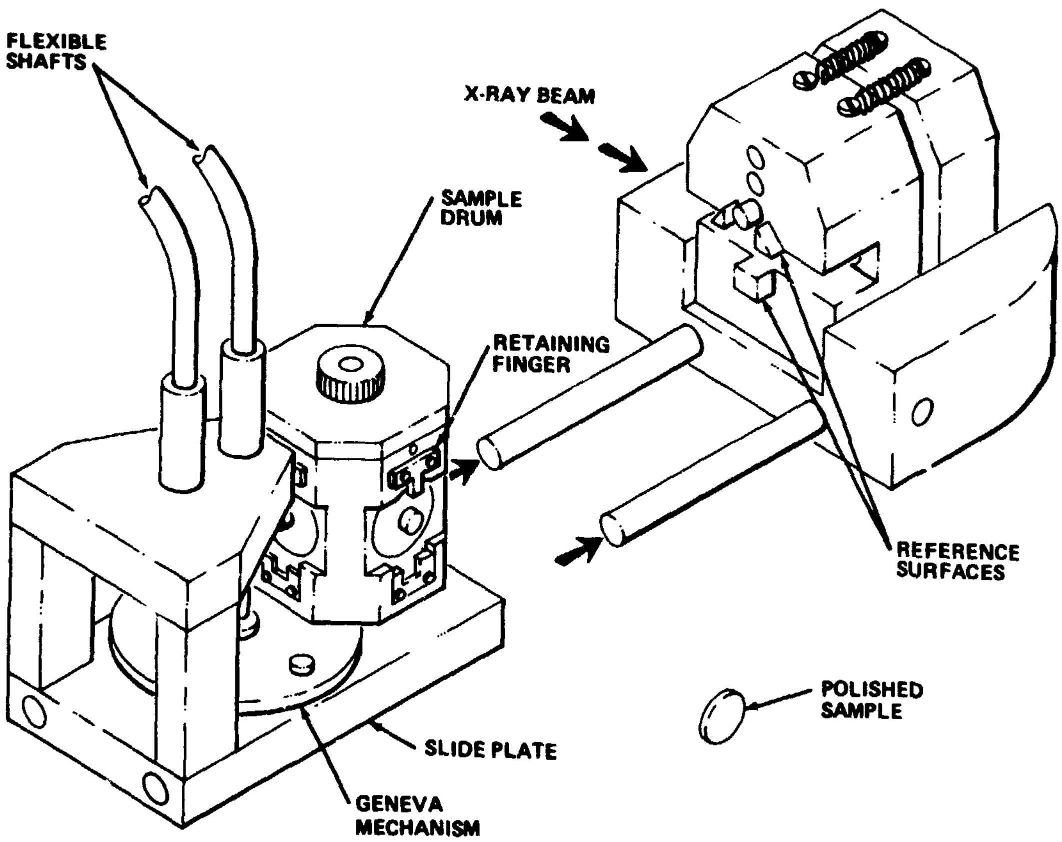

Figure 6. Multiple sample holder.

drum rotates on a vertical shaft and is driven by a four-place Geneva mechanism. A Geneva mechanism is used so that the rotational positioning of the sample drum is fairly independent of the final positioning of the flexible shaft which turns the Geneva driver wheel. The sample drum, in fact, remains in the proper position and locked for any stopping orientation of the flexible shaft over a range of at least 90°.

Once the sample drum has been rotated so that the desired sample is in position, the sample must be moved into the x-ray beam and held in proper alignment. This motion is accomplished by sliding the sample drum forward until the polished face of the sample contacts the three reference surfaces. Motion is continued slightly beyond first contact, compressing the spring behind the sample, to insure firm contact with all three reference surfaces.

The sample holder is mounted on a precision divided circle clinometer. The angle of the sample with respect to the direct beam can be read on a scale divided at intervals of 0.2 sec of arc. The sample can be remotely rotated through 90° and its position remotely read by a fiber optics light pipe.

The x-ray reflectometer has three slits: collimating slit, monitor slit, and sample detector slit. The openings of the slit to the proper width are measured by micrometers. The collimating slit is located between the micro-focus source and the crystal and its jaws are independently adjustable for defining the x-ray beam. The purpose of this slit is to limit the divergence of the beam to a few arc seconds. The monitor slit is located between the crystal and the movable monitor counter and its jaws also are independently adjustable. The purpose of the monitor slit is to confine the x-rays to the face of the sample being measured. The sample detector slit has two adjustments, one for the size of the slit opening and the other for a translation adjustment. This slit, located in front of the sample detector, has two positions of operation. In Figure 7 the

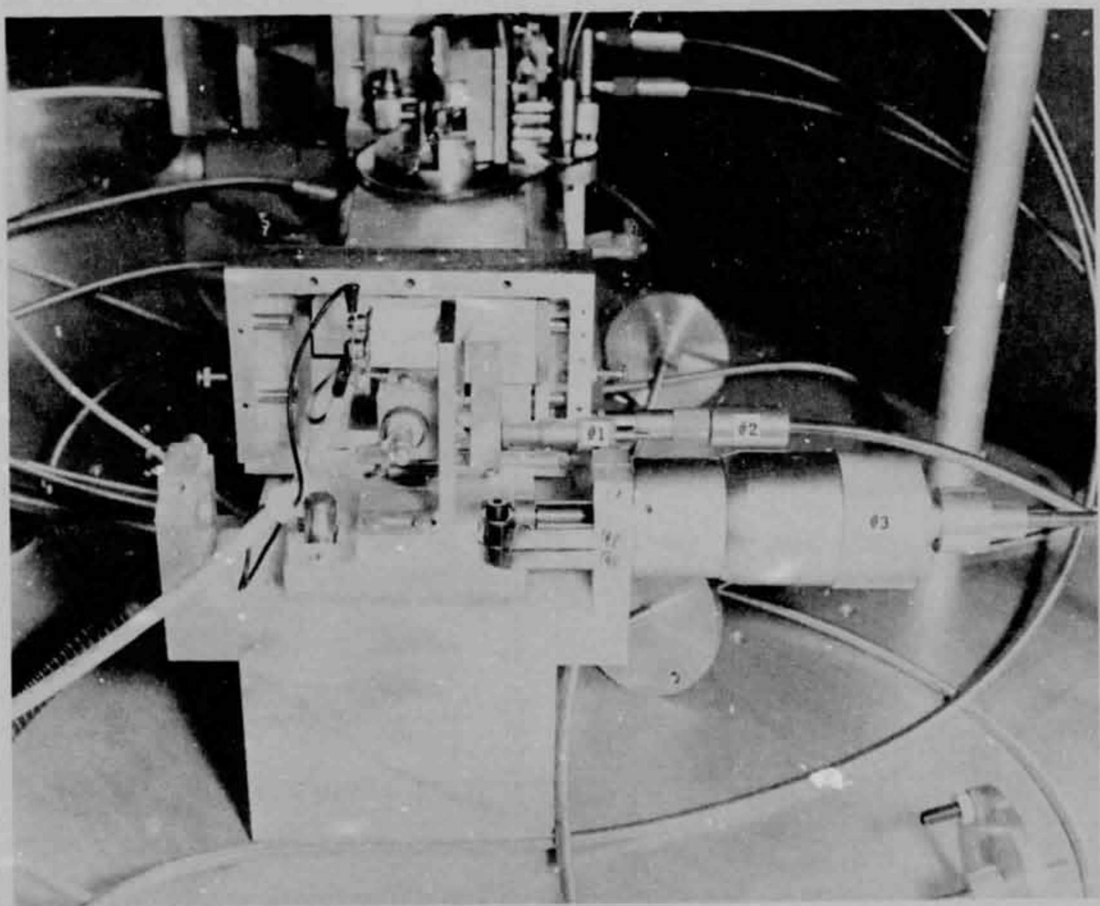

Figure 7. Detector and detector-slit assembly.

narrow slit opening is adjustable using micrometer #1, and the entire slit is translated using micrometer #2. The circular opening in this slit housing is slightly less than the diameter of the detector window. The total reflectivity measurements were taken with the large opening positioned in front of the sample detector. The angular distribution of the x-ray beam is measured by closing the jaws of the sample detector slit to a width small compared to the linear extent of the reflected x-ray beam in the detector plane. The narrow slit opening is then translated to the center of the detector face. The detector and slit assembly is stepped across the reflected x-ray beam in increments to measure the profile of the beam. The position of the slit assembly in relation to the detector for each of the measurements is shown schematically in Figure 8.

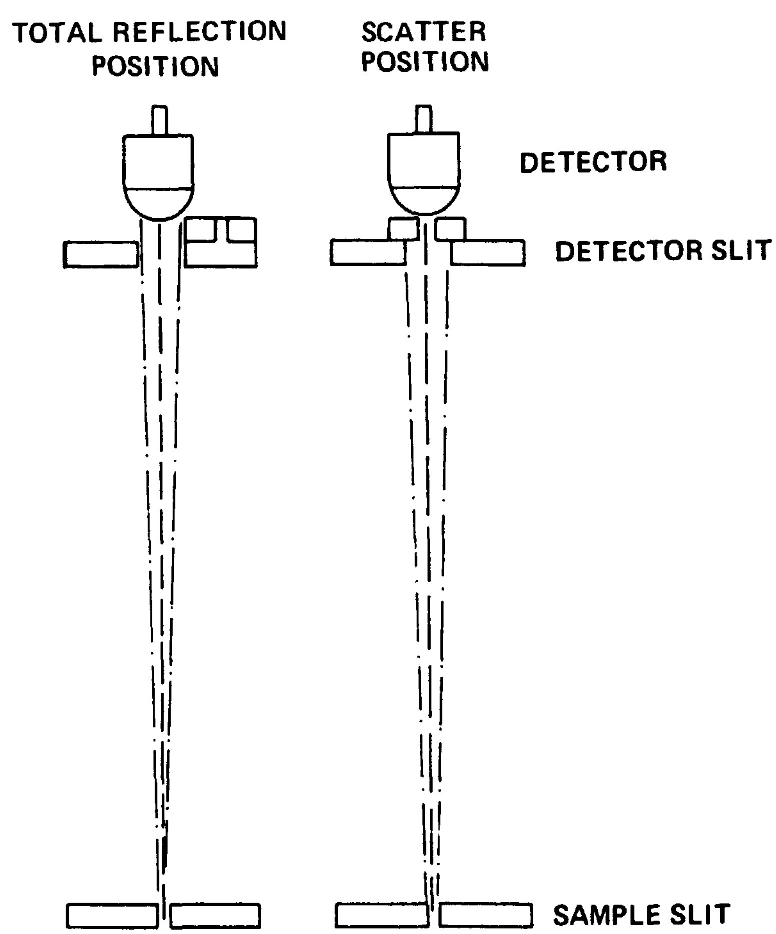

Figure 8. Schematic of detector-slit arrangement.

The vacuum x-ray reflectometer uses two detectors during operation. The detectors used in these measurements were geiger counters with a 1.5 mg/cm mica window filled to a pressure of 9.1×10^4 N/m^2 with argon and halogen gas. One of the detectors is mounted in front of the sample. The purpose of this detector is to monitor the radiation that is striking the sample surface. The second detector is mounted on two arms, both pivoted at the axis of the sample turntable. The purpose of the larger arm (the one resting on the baseplate) is to provide rough positioning of the detector during initial alignment and also in remote operation. The smaller arm, the one to which the detector and detector slit are attached, provides for fine positioning and scanning of the detector through the x-ray beam reflected from the sample, thus giving the angular profile of the beam. This motion is obtained by rotation of micrometer #3 in Figure 7. The fine position arm is movable through a 10-deg arc.

B. Data Processing Equipment

The signal received by the detectors is transmitted outside of the chamber. The signal passes through standard x-ray instruments and into a programmable calculator that controls peripheral equipment. The peripheral equipment is an X-Y plotter, multichannel analyzer (MCA), and a printer (Figure 9).

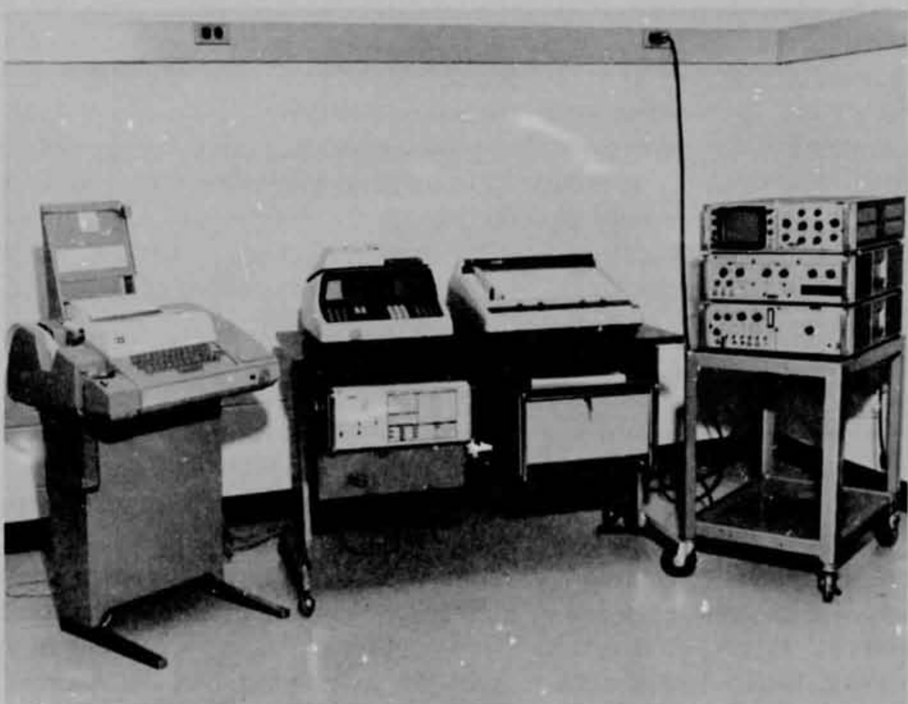

Figure 9. Data processing system.

The data are accumulated for each data point on the basis of time as determined by the program in the calculator. For the accumulation of data for one data point, the following sequence is used. The data are accumulated for 5 s in the first channel of the MCA, then accumulation begins in the second channel. This sequence continues until 10 channels of 5 s each have been used, or a total of 50 s of time. The data are read from the MCA into the calculator, averaged, radiation background subtracted, and printed out with appropriate headings. Also, during this operation, the data are plotted at a convenient scale and stored in the MCA for further analysis after accumulation of all data.

III. TYPE OF MEASUREMENTS

The measurements reported here are for an x-ray source with an aluminum anode generating 8.34Å x-rays. Two types of measurements are discussed in this report: total reflection measurements and scatter measurements.

A. Total Reflection

The total reflection measurements are made by positioning the open portion of the sample detector slit in front of the sample detector so that all of the reflected radiation will strike the detector face. With the slit in this position all radiation reflected by the sample within a half angle of 1.5° will strike the face of the detector. The monitor and sample detector are calibrated and are used alternately to monitor the incident x-ray beam and the reflected beam. The x-ray counts are passed through the data processor and result in a plot of the reflection efficiency as a function of angle of incidence, as well as a printout of this information. Normally the data were taken at angles of incidence in 5 arc min steps and terminated when the reflection efficiency decreased below 1 percent.

A computer program was prepared to calculate the x-ray reflectivity as a function of the angle of incidence for plane surfaces as well as multilaminate planar surfaces [2]. The program calculates the real and imaginary components, δ and β, of the complex index of refraction from the more readily accessible physical parameters such as density, x-ray absorption coefficients and their wavelength dependence, atomic level oscillator strengths, and other parameters. Having determined δ and β and knowing the thickness of the layer, the program then calculates the reflectance as a function of the angle of incidence. The calculated reflection efficiency curve is given for each clean sample measured.

B. X-Ray Scatter

The scatter measurements were made by placing a 2.3 arc sec slit in front of the sample detector and stepping through the reflected x-ray beam. Since the sample detector slit assembly can be translated from the open position to the narrow slit position, reflection and scatter measurements can be alternately made without changing the angular opening of the scatter slit. Most of the scatter measurements were taken by stepping the sample detector at 1.15 arc sec increments through the reflected x-ray beam. The detector operated at each position for 50 s with the data being processed, stored in the MCA, and plotted as desired. It was found that an angular scan range of 54 arc sec was adequate for most of the samples. The scatter data were taken for most samples at an angle of incidence (θ) of 50 arc min. Either before or after measuring the scatter curve for each sample, the sample was removed from the x-ray beam and the sample detector was stepped through the unreflected beam. These data would then allow the reflected and unreflected beams to be compared to determine the effect of the sample on the beam.

As the sample detector was stepped through the x-ray beam, the count rate would vary from near zero to a peak near the midpoint of the traverse and then drop to near zero as the edge of the beam was approached. This resulted in a curve defined by a set of points which were spaced 1.15 arc sec on the x-axis. For plotting purposes the data were normalized to the peak intensity of the x-ray beam. Because of the spread in the data, a computer program was prepared for smoothing of the intensity (y) as a function of beam width (x) by conventional least squares theory which can be found in almost any text on numerical analysis [3, 4].

The basis for the least squares theory applied in this study is the one which requires that the sum of the squares of the deviations of the data from the smooth curve be a minimum in the y direction only.

To satisfy the previously mentioned basic requirements exactly, it is necessary to vary the functions selected for the smooth curve over the entire function space, calculate the rms for each function, and pick the function with the minimum rms or select a function which will go through all the data points, thus giving a zero deviation. Neither of these was applied since the first is impossible and the last is disinteresting for a large set of data points. For this reason, the exact minimum was not required.

The actual criteria used required that the rms deviation be a minimum to 8 significant digits for the functions selected a priori.

The class of functions selected was fourth degree polynomial exponentials of the form,

$$y = \exp(ax^4 + bx^3 + cx^2 + dx + c) \quad . \tag{1}$$

The deviation for the ith data point is

$$d_i = y_i - \exp(ax^4 + bx^3 + cx^2 + dx + c) \equiv p_4(x) \quad . \tag{2}$$

The sum of the squares of the deviations is then

$$s = \sum [y_i - \exp(ax_i^4 + bx_i^3 + cx_i^2 + dx_i + e)]^2 \quad . \tag{3}$$

The minimum of s is found by equating the partial derivatives of s with respect to a, b, c, d, and e to zero and solving the resulting system of equations for the values of a, b, c, d, and e gives:

$$\begin{aligned}
\sum y_i x_i^4 \exp(P_4(x_i)) &= \sum x_i^4 \exp(2P_4(x_i)) \\
\sum y_i x_i^3 \exp(P_4(x_i)) &= \sum x_i^3 \exp(2P_4(x_i)) \\
\sum y_i x_i^2 \exp(P_4(x_i)) &= \sum x_i^2 \exp(2P_4(x_i)) \\
\sum y_i x_i \exp(P_4(x_i)) &= \sum x_i \exp(2P_4(x_i)) \\
\sum y_i \exp(P_4(x_i)) &= \sum x_i \exp(2P_4(x_i)) \quad .
\end{aligned} \tag{4}$$

These must now be solved for the coefficients a, b, c, d, and e. Since this system is nonlinear, it is necessary to apply an iterative scheme which requires long computing time. Therefore, this system was not used to find the minimum. Instead, the natural logarithm technique was applied to equation (1), so that the deviation becomes

$$d_i = \mathrm{LN}\, y_i - P_4(x_i) \quad , \tag{5}$$

and s is now

$$S = \sum (\mathrm{LN}\, y_i - P_4(x_i))^2 \quad . \tag{6}$$

The partial derivatives with respect to a, b, c, d, and e now give

$$\begin{pmatrix} \sum x_i^8 & \sum x_i^7 & \sum x_i^6 & \sum x_i^5 & \sum x_i^4 \\ \sum x_i^7 & \sum x_i^6 & \sum x_i^5 & \sum x_i^4 & \sum x_i^3 \\ \sum x_i^6 & \sum x_i^5 & \sum x_i^4 & \sum x_i^3 & \sum x_i^2 \\ \sum x_i^5 & \sum x_i^4 & \sum x_i^3 & \sum x_i^2 & \sum x_i \\ \sum x_i^4 & \sum x_i^3 & \sum x_i^2 & \sum x_i & \sum N \end{pmatrix} \begin{pmatrix} a \\ b \\ c \\ d \\ e \end{pmatrix} = \begin{pmatrix} \sum x_i^4\, \mathrm{LN}\, y_i \\ \sum x_i^3\, \mathrm{LN}\, y_i \\ \sum x_i^2\, \mathrm{LN}\, y_i \\ \sum x_i\, \mathrm{LN}\, y_i \\ \sum \mathrm{LN}\, y_i \end{pmatrix} \tag{7}$$

From this system it is noted that symmetrical x data will give zeros for all the odd-powered coefficients. For this reason the experimental data were taken centered about $X = 0$. This allowed the decoupling of the system in equation (7) so that a 2×2 and 3×3 matrix could be solved instead of a 5×5. This was desirable since the computer used was limited in programming steps.

It should be noted that the deviation is defined as the difference between the logarithm of the function and the logarithmic data rather than the difference between the function and the data. The relationship of the two is

$$d_f = y\,(1 - e^{-d_L}) \tag{8}$$

where d_f is the difference in the function and the data and d_L is the difference in the logarithm of the function and the logarithm of the data.

It may be observed that the two agree only at zero deviation; thus, the method should give good results for small deviations but will not work well for larger ones (i.e., scattered data).

The data were normalized to the maximum value of y; therefore, the upper limits for the error can be visualized from the plot in Figure 10.

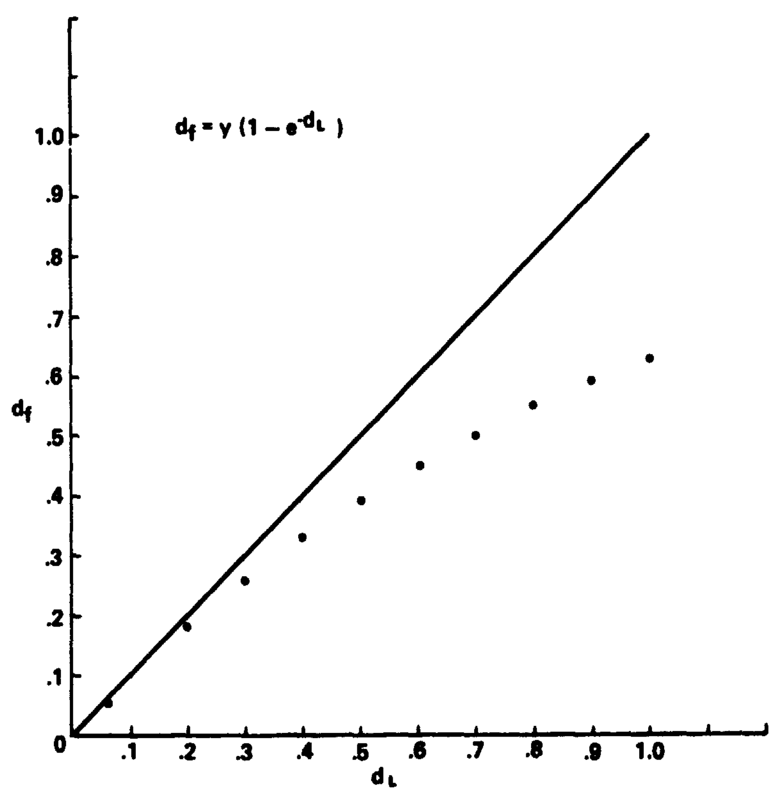

Figure 10. Relative error between d_f and d_L.

The numerical values of the coefficients a, b, c, d, and e are given in Table 1 and are identified by the sample number and the figures in which the curves appear.

TABLE 1. NUMERICAL COEFFICIENTS

Figure No.	Sample No.	a	b	c	d	e
12, 14	1	-1.961×10^{-5}	1.455×10^{-7}	1.626×10^{-2}	-1.047×10^{-2}	
13, 14	unr. beam*	-2.228×10^{-5}	-8.116×10^{-4}	1.634×10^{-2}	7.915×10^{-3}	
13, 15, 16	2	-2.040×10^{-5}	2.588×10^{-6}	1.609×10^{-2}	-1.901×10^{-2}	
18, 20	3	-1.874×10^{-5}	3.714×10^{-6}	1.631×10^{-2}	-1.875×10^{-2}	
19, 20	unr. beam	-1.993×10^{-5}	2.265×10^{-5}	1.683×10^{-2}	-5.948×10^{-3}	
22, 24, 30	4	-1.941×10^{-5}	1.546×10^{-4}	1.495×10^{-2}	-5.584×10^{-2}	
23, 24	unr. beam	-2.014×10^{-5}	6.6787×10^{-5}	1.625×10^{-2}	-2.928×10^{-2}	
28, 29, 30, 40	4 (cont)**	-1.845×10^{-5}	-1.438×10^{-6}	1.423×10^{-2}	-5.442×10^{-3}	
29, 33, 38	unr. beam	-2.011×10^{-5}	3.621×10^{-7}	1.747×10^{-2}	7.213×10^{-3}	
32, 33, 39	5	-2.479×10^{-5}	1.251×10^{-5}	1.633×10^{-2}	-5.235×10^{-3}	
37, 38, 39, 40	5 (cont)	-1.297×10^{-5}	2.854×10^{-5}	1.067×10^{-2}	-1.133×10^{-2}	
44, 58	6	-2.513×10^{-5}	-1.202×10^{-4}	2.093×10^{-2}	3.070×10^{-2}	
45, 59	6	-2.432×10^{-5}	-1.575×10^{-5}	1.766×10^{-2}	-1.138×10^{-2}	
46, 60	6	-7.689×10^{-6}	-4.317×10^{-6}	2.925×10^{-2}	6.241×10^{-3}	
47, 61	6	2.176×10^{-5}	-4.009×10^{-5}	1.664×10^{-2}	-2.93×10^{-3}	
48	unr. beam	-2.465×10^{-5}	2.165×10^{-6}	2.1066×10^{-2}	6.803×10^{-2}	
52, 57	6 (cont)	1.512×10^{-5}	-4.55×10^{-4}	4.978×10^{-3}	9.558×10^{-2}	0.63197
53, 58	6 (cont)	-1.585×10^{-5}	1.123×10^{-4}	1.376×10^{-2}	-4.712×10^{-2}	
54, 59	6 (cont)	-2.192×10^{-5}	-8.922×10^{-5}	1.6774×10^{-2}	3.676×10^{-2}	
43, 57	6	-1.683×10^{-5}	-4.106×10^{-4}	1.566×10^{-2}	0.121	
55, 60	6 (cont)	-2.152×10^{-5}	-4.656×10^{-5}	1.555×10^{-2}	9.524×10^{-3}	
56, 61	6 (cont)	-1.753×10^{-5}	-1.074×10^{-5}	1.425×10^{-2}	-1.006×10^{-2}	
65, 67, 68	7 (cont)	-1.9009×10^{-5}	4.123×10^{-5}	1.582×10^{-2}	-2.562×10^{-2}	
67, 73, 74	8	-2.1448×10^{-5}	8.660×10^{-5}	1.789×10^{-2}	-4.582×10^{-2}	
68	unr. beam	-1.7709×10^{-5}	8.244×10^{-5}	1.574×10^{-2}	-2.906×10^{-2}	
74, 75	8 (cont)	-1.407×10^{-5}	-1.458×10^{-4}	1.108×10^{-2}	-6.515×10^{-3}	
75	unr. beam	-1.853×10^{-5}	6.732×10^{-5}	1.671×10^{-2}	-1.568×10^{-2}	

* Unreflected Beam
** Contaminated

IV. DESCRIPTION OF SAMPLES AND RESULTS

The samples which will be discussed in this report are all 2.54 cm diameter optical flats 0.635 cm thick. Sixty fused silica samples were purchased in one order. The 60 samples were specified to be finished to a flatness of $\lambda/10$. Twenty of these samples were selected for measuring the optical properties of fused silica at x-ray wavelengths. Twenty were selected and coated with 99.999 percent purity nickel to a thickness of 1000Å ± 25Å. The remaining 20 were coated with 99.999 percent purity chromium to a thickness of 1000Å ± 25Å. The measurements which have been made on selected samples from the original 60 will be discussed in terms of the reflecting surface.

All of the samples were cleaned before measuring. Selected samples were then contaminated and remeasured to determine the effect of the contaminant on the scatter and reflection properties. In this report the sample carries the same identification number regardless of the number of tests or the conditions of the sample.

A. Fused Silica

1. Sample #1. This sample was cleaned and measured to determine the scatter characteristics. The data were taken at an angle of incidence $\theta = 50$ arc min, where θ is the angle between the incident radiation and the reflecting surface as shown in Figure 11. The experimental data are plotted in

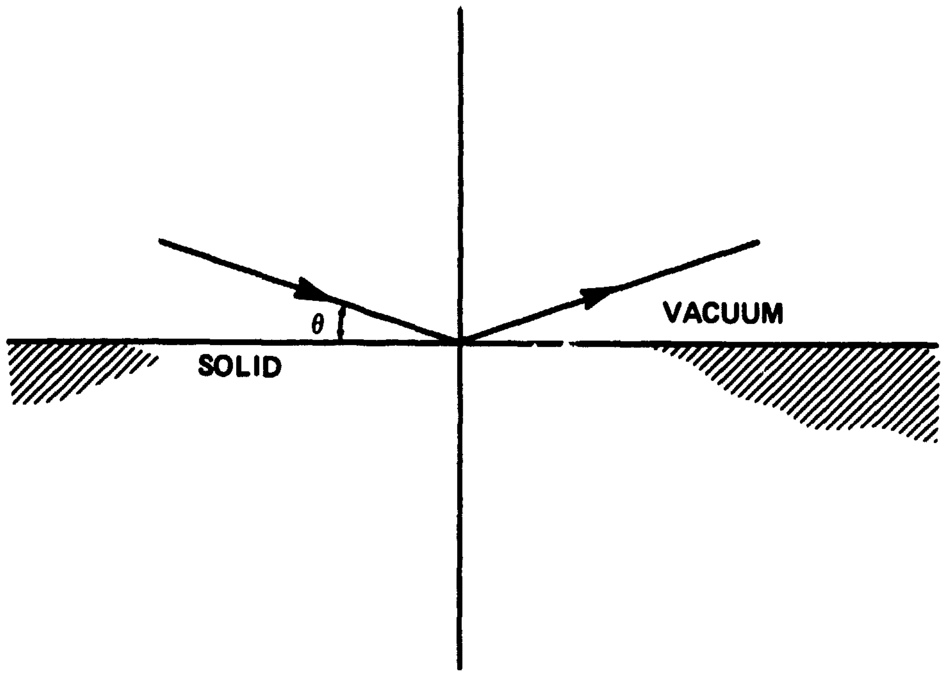

Figure 11. Angle of incidence θ.

Figure 12 with the relative intensity of the reflected x-ray beam as a function of the angular distance of the detector away from the position of peak intensity. The experimental data are shown as circles and the least squares curve fit as a solid curve. The full-width-at-half-maximum (FWHM) of the reflected x-ray beam as defined by the smooth data is 13.45 arc sec. The scatter curve for the unreflected x-ray beam is given in Figure 13. The angular spread of the

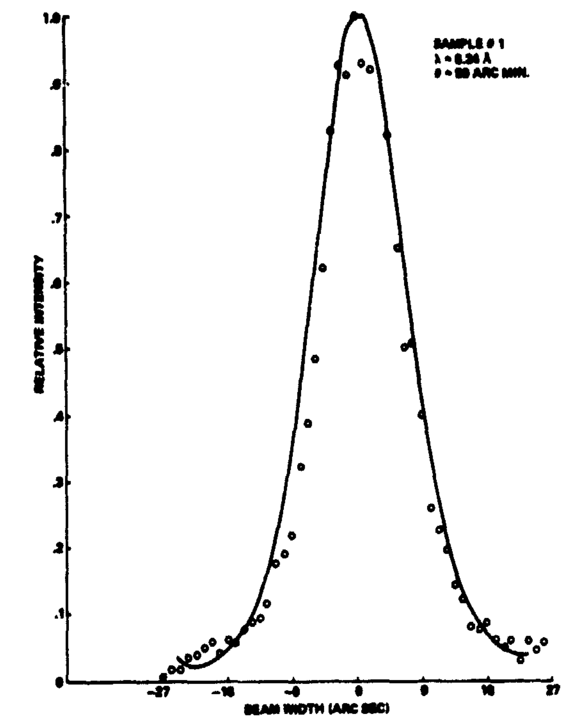

Figure 12. Fused silica sample #1, θ = 50 arc min.

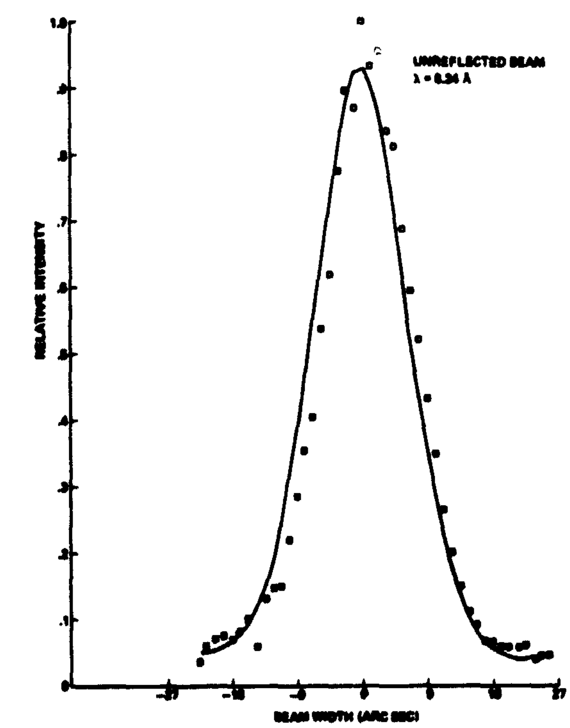

Figure 13. Unreflected x-ray beam for samples #1 and #2.

unreflected beam at the FWHM is 13.46 arc sec. Figure 14 is a comparison of the x-ray beam reflected by the fused silica sample and the unreflected beam. The sample reflected the x-ray beam without increasing the angular extent of the beam, indicating a good reflecting surface within the resolution of the x-ray reflectometer. In fact, the change in the FWHM is within the experimental error of the system. Unfortunately, the schedule did not permit the total reflection measurements to be completed on this sample.

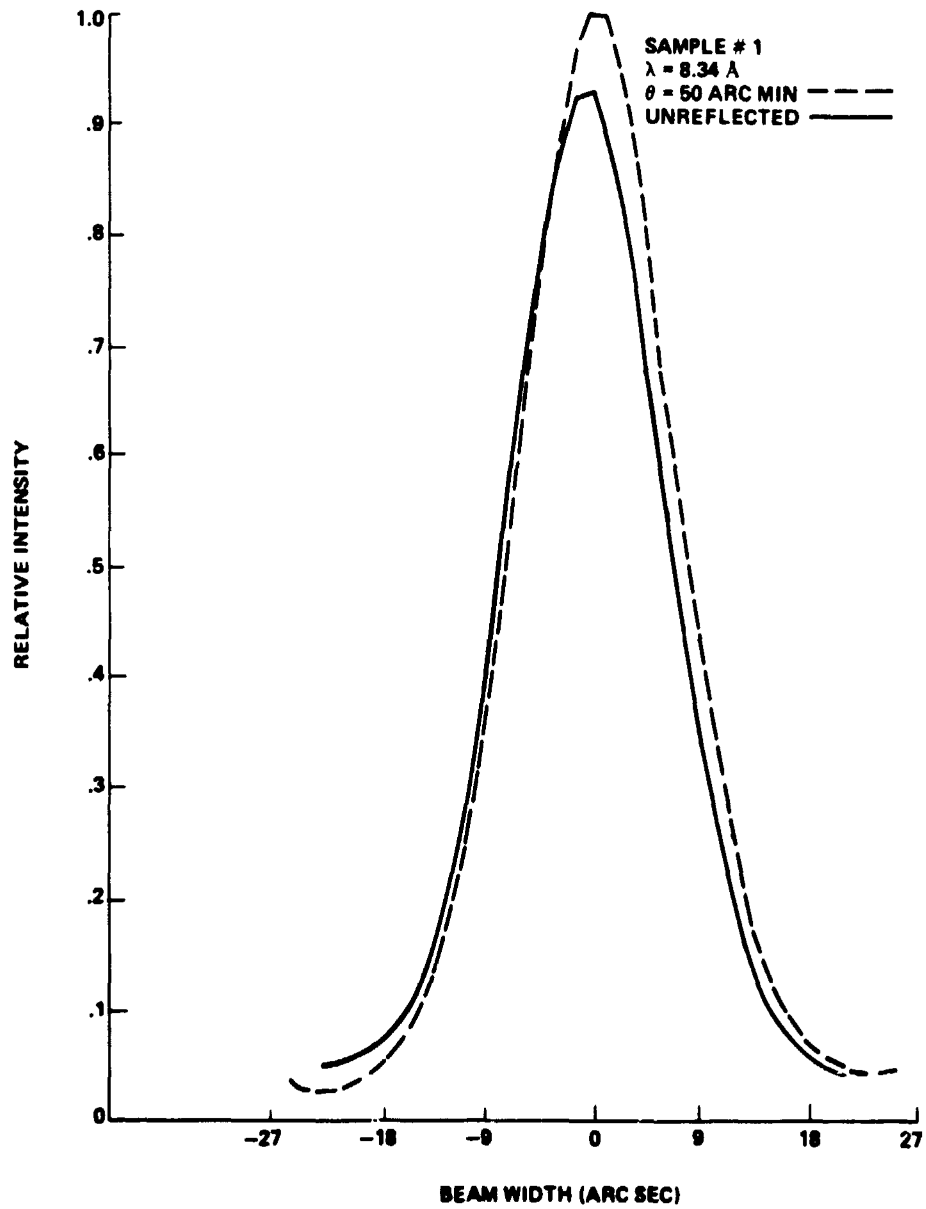

Figure 14. Comparison of sample #1 and unreflected beam.

2. Sample #2. This sample was cleaned and measured at the same time as sample #1. As with sample #1, the only measurement was to determine the scatter curve at an angle of incidence of 50 arc min. The scatter curve is given in Figure 15 and has a FWHM value of 13.65 arc sec. The reflection efficiency at θ = 50 arc min determined by comparing the area under the curve for the reflected and unreflected x-ray beam is 87 percent. The x-ray data

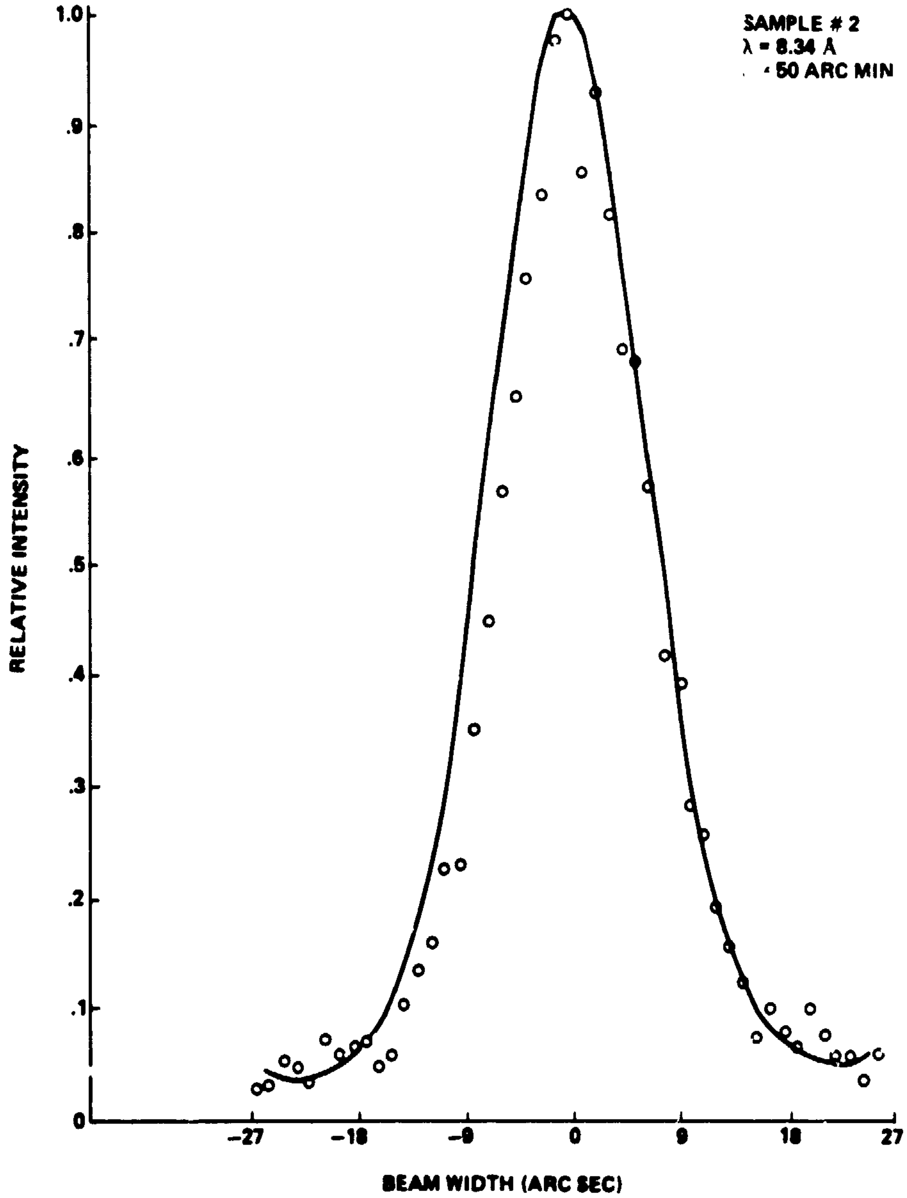

Figure 15. Fused silica sample #2, θ = 50 arc min.

reflected by the sample are compared to the unreflected x-ray beam in Figure 16. Again, the increase in the angular extent of the beam is very small, indicating a good reflecting surface at this wavelength.

3. Sample #3. This sample was used as a control sample during the measuring of samples #4 and #5 which were measured under two conditions. All three samples were cleaned and measured during one pump down. Samples #4 and #5 were removed from the sample drum, contaminated, replaced in the drum, and remeasured. Sample #3 remained in the drum to serve as a standard so that

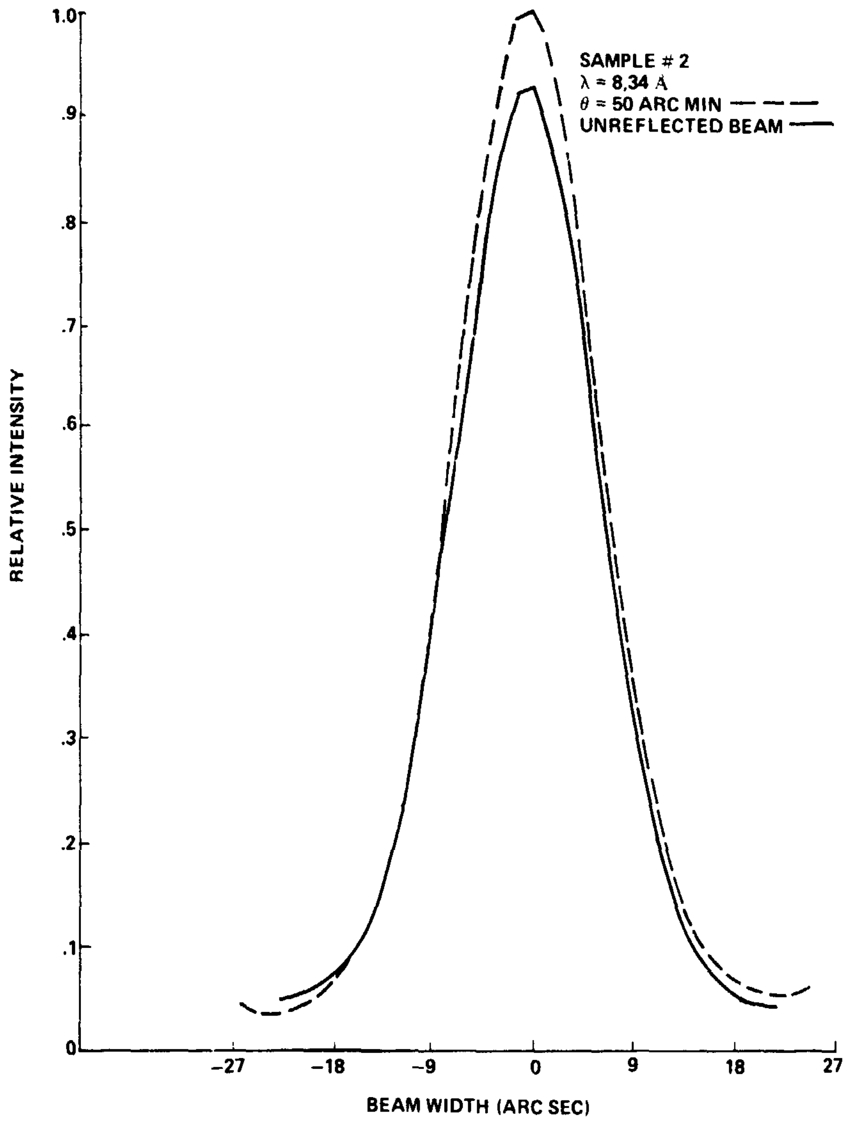

Figure 16. Comparison of sample #2 and unreflected beam.

the change in the measurements due to the contamination could be identified. Figure 17 is the reflection efficiency curve for sample #3 averaged for the two tests. The solid line is the theoretical reflection efficiency for fused silica. The experimental data agree reasonably well with the theoretical data at angles of incidence less than the critical angle with the spread between the theoretical and experimental greatest at $\theta = 60$ arc min or in the portion of the curve where the slope is greatest. The scatter curve for the two measurements on sample #3 is given in Figure 18 for $\theta = 50$ arc min.

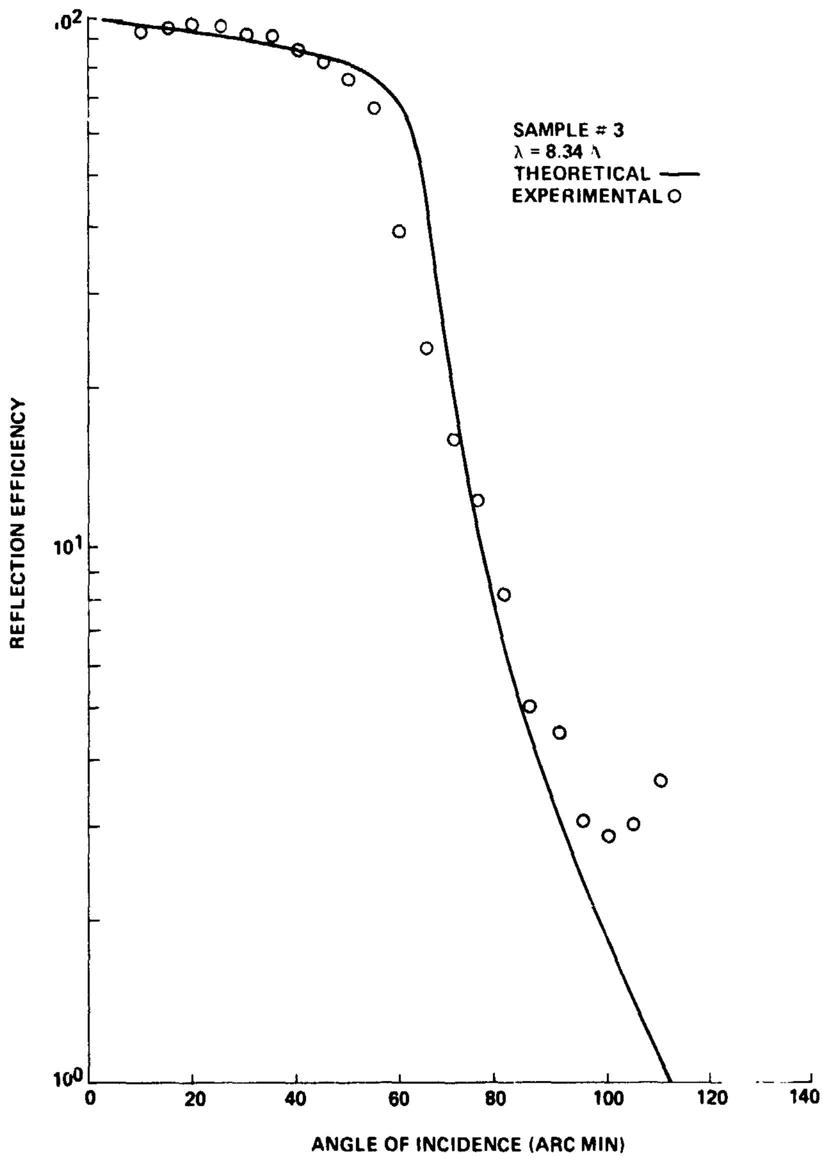

Figure 17. Reflection efficiency for fused silica sample #2.

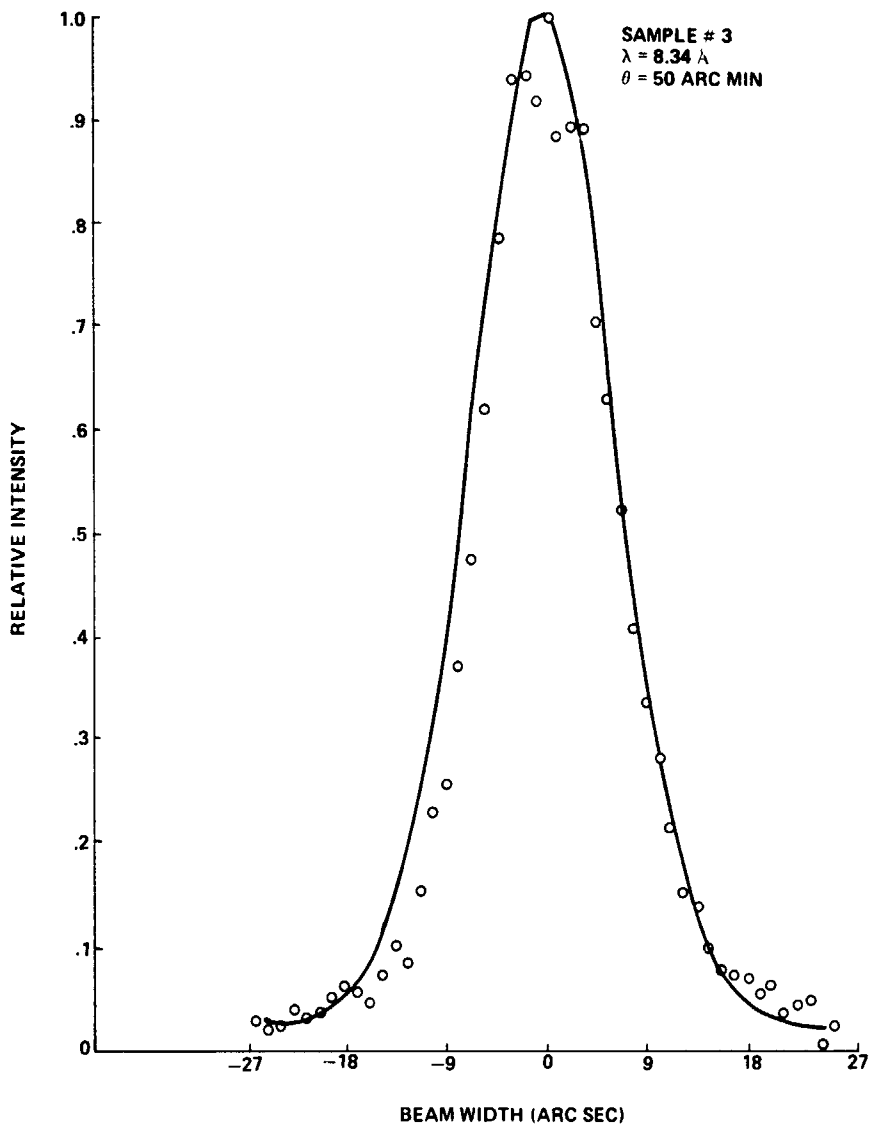

Figure 18. Fused silica sample #3, θ = 50 arc min.

The FWHM of the scatter curve is 13.43 arc sec. The unreflected beam for the two measurements of sample #3 is plotted in Figure 19 with a FWHM of 13.18 arc sec. The two curves are compared in Figure 20. It is obvious from this plot that this sample had very little effect on the x-ray beam either at the FWHM point or in the wings of the curve. Therefore, this measurement indicated that this sample contains a good optical surface for this wavelength radiation.

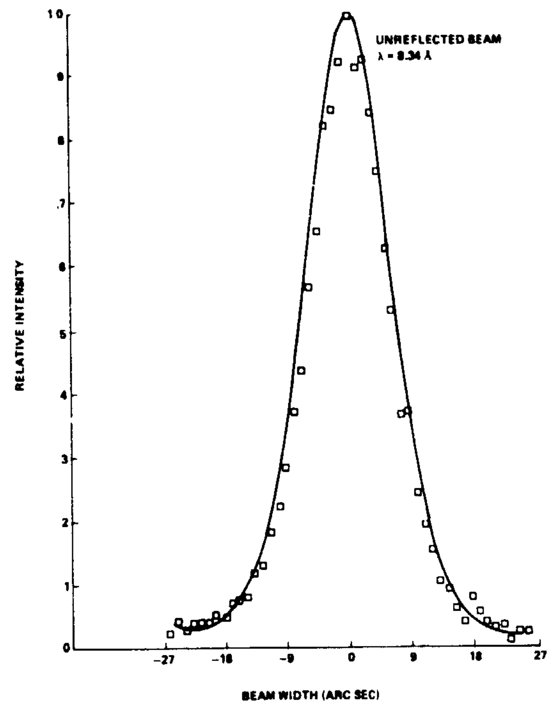

Figure 19. Unreflected x-ray beam for samples #3, 4, and 5.

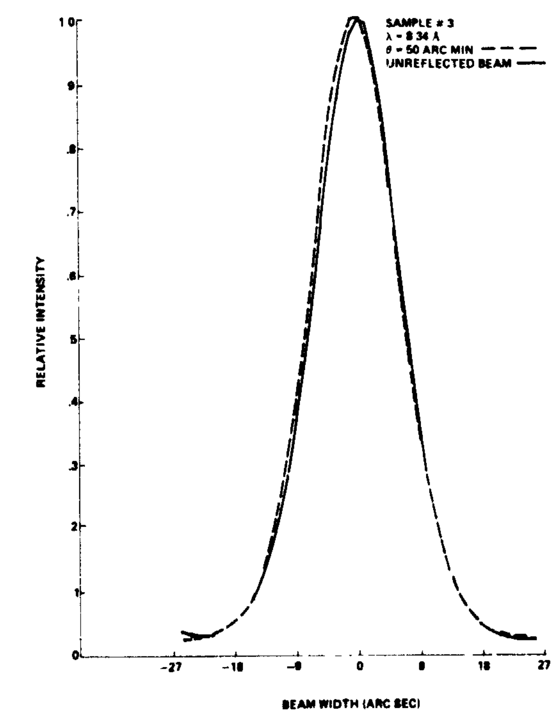

Figure 20. Comparison of sample #3 and unreflected beam.

4. Sample #4. This fused silica sample was cleaned and measured and then contaminated with 10 μm diameter carbon particles and remeasured.

The reflection efficiency curve for the clean sample is given in Figure 21 together with the theoretical curve. Again, the experimental data agree very well with the theoretical curve at angles less than the critical angle, with the greatest difference being at $\theta = 60$ arc min where the experimental data are considerably lower than the theoretical data.

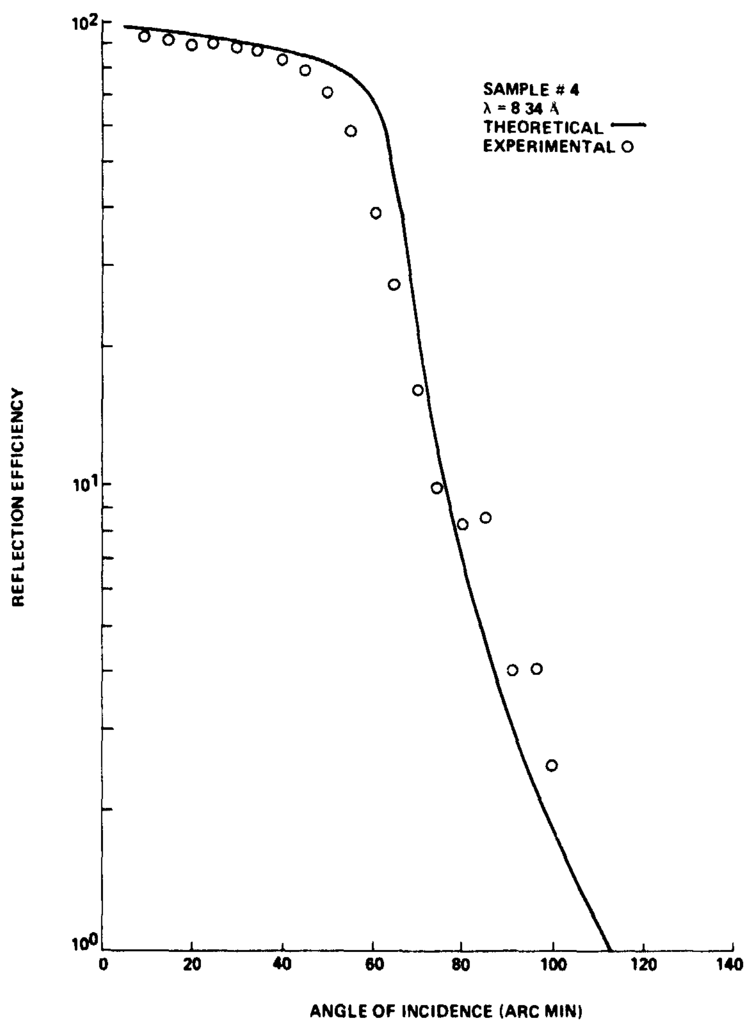

Figure 21. Reflection efficiency for fused silica sample #4.

The scatter curve is given in Figure 22 for this sample at θ = 50 arc min. The FWHM is 14.38 arc sec. The unreflected beam measured with the tests on samples #4 and #5 is given in Figure 23 with a FWHM of 13.56 arc sec. The scatter curve for sample #4 is compared to the unreflected beam in Figure 24. The angular increase of 0.82 arc sec in the reflected x-ray beam indicates that this sample is a good reflector of 8.34 Å x-rays.

After the sample was measured in a clean condition, it was contaminated with carbon particles to an average density of 189 particles/mm^2. The particle size distribution is shown in Figure 25. The particles ranged in size from 1 to

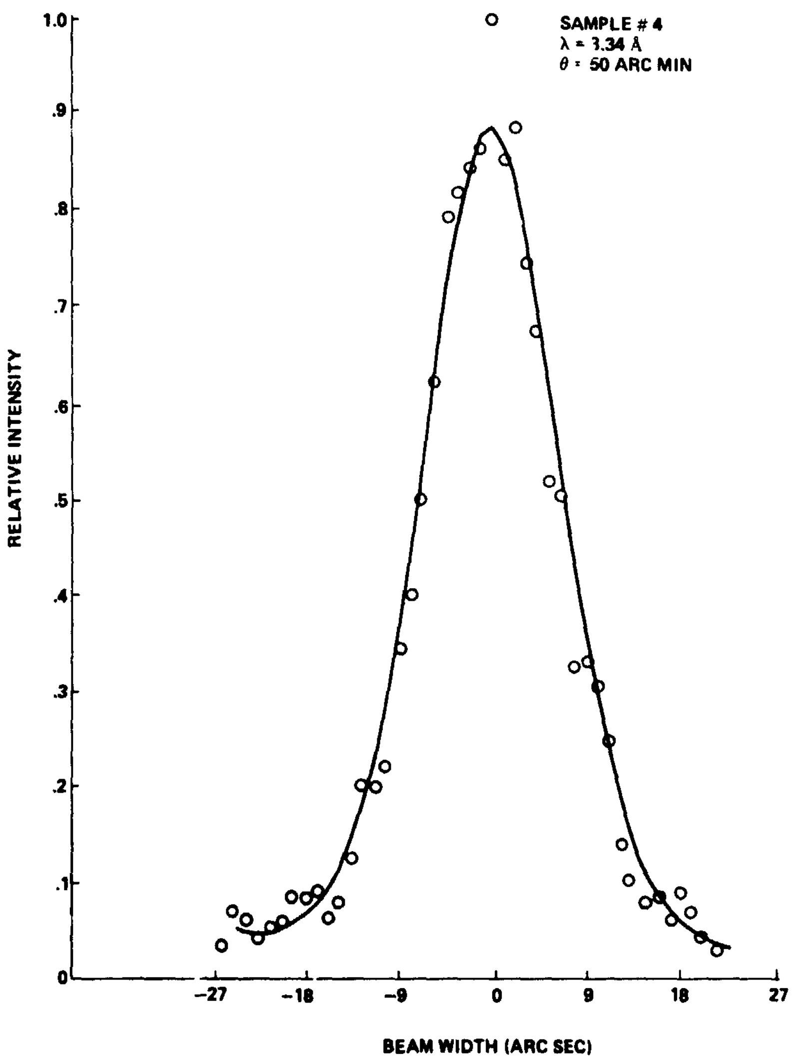

Figure 22. Fused silica sample #4, θ = 50 arc min.

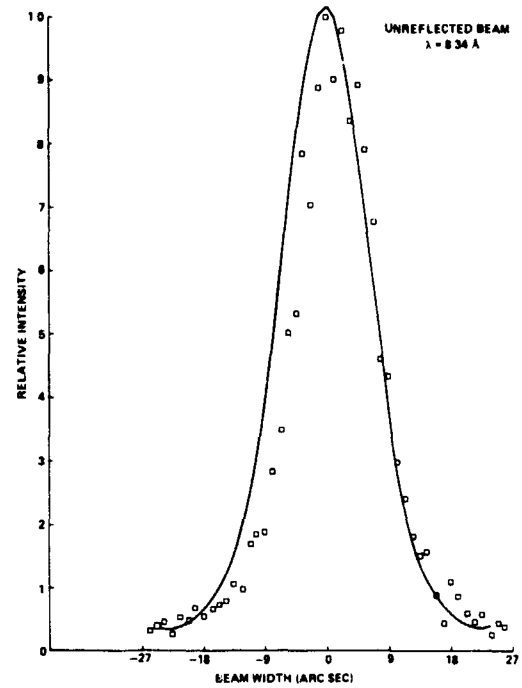

Figure 23. Unreflected x-ray beam for samples #4 and #5.

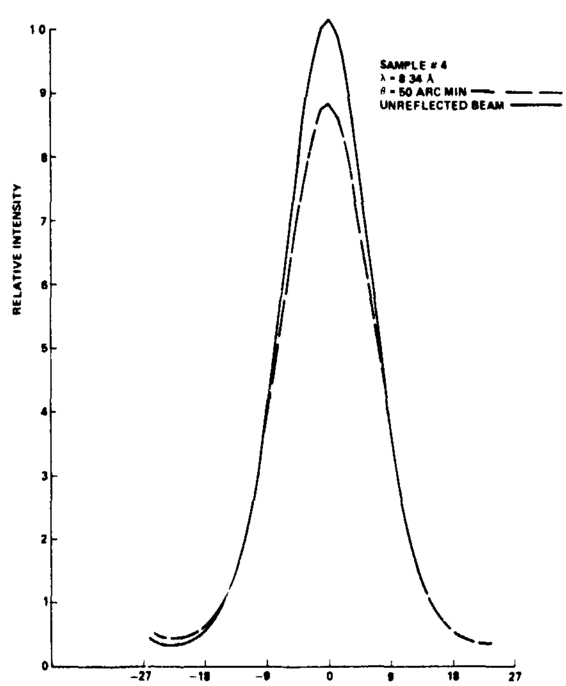

Figure 24. Comparison of sample #4 and unreflected beam.

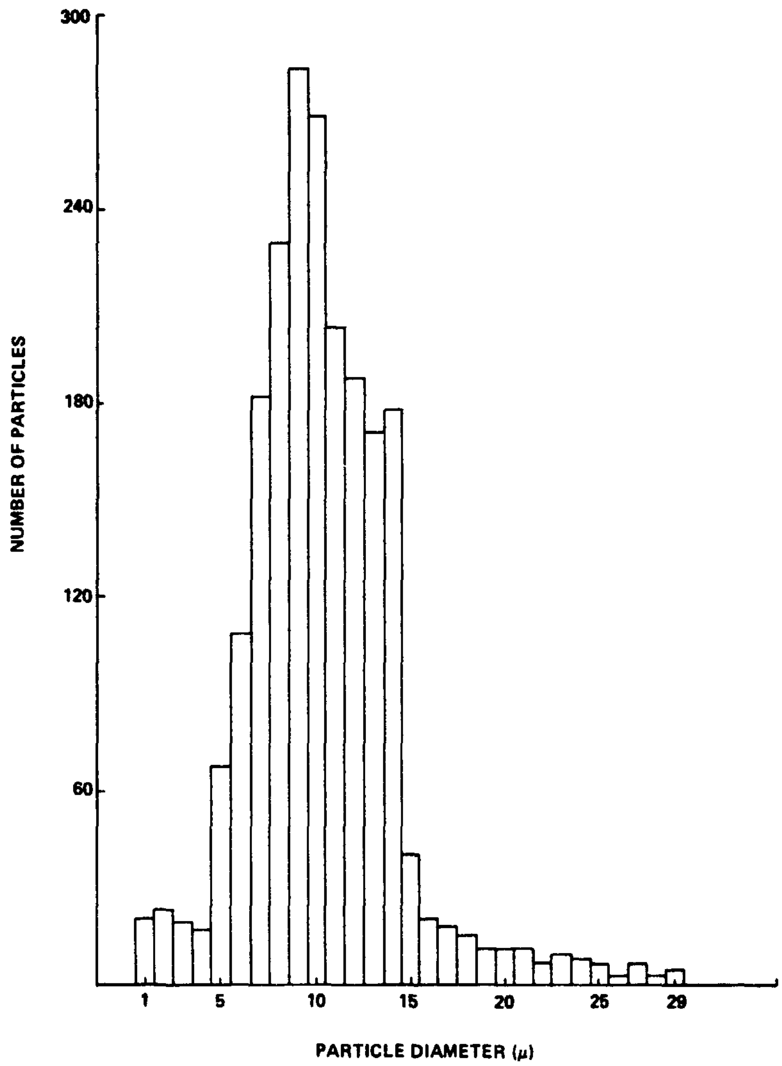

Figure 25. Size distribution of carbon particles on sample #4.

29 μm in diameter, with the largest number of particles in the 9 μm diameter range. Twenty areas of the surface were inspected for a total area of 1.092×10^7 μm^2 and a total particle count of 2070. A microphotograph of the sample after the carbon particles were applied is shown in Figure 26.

The measurements on the contaminated sample #4 were made with the control sample #3 in the sample drum so that the measurements between the clean and contaminated sample #4 could be adjusted to reflect only those effects

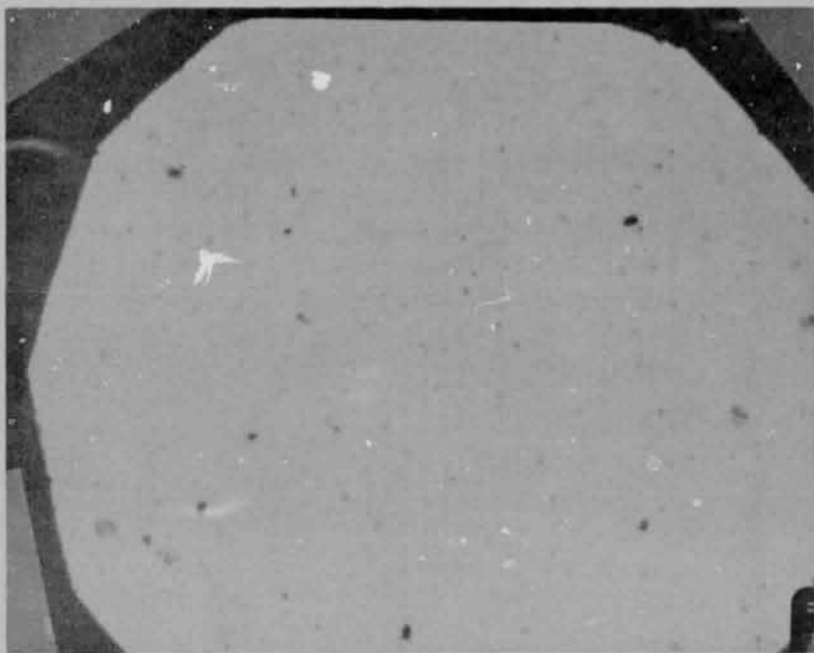

Figure 26. Sample #4 after depositing carbon particles.

caused by the contamination. Figure 27 shows the reflection efficiency curve corrected to indicate only the changes due to the particle contamination. Also shown is the reflection efficiency curve for the clean sample. The efficiency of the contaminated sample was 74 percent at $\theta = 10$ arc min, which is the minimum angle that reflection data can be taken with our reflectometer. This is a decrease in efficiency of 20 percent from the clean sample. The efficiency decreases to 64 percent at $\theta = 20$ arc min, which is the maximum difference between the two curves. The efficiency is down at this point by 34 percent. The efficiency increases as θ increases to 40 arc min, at which point the contaminated efficiency is only about 5 percent below the clean sample. From the critical angle to larger angles the efficiency of the two surfaces are similar. The maximum decrease in the reflection efficiency for an optical surface contaminated with particulate material would be expected to occur at the smaller values of θ since the projected area of the particle onto the surface would be greatest at small values of θ.

The scatter curve for the contaminated sample at $\theta = 50$ arc min is given in Figure 28, and is compared to the unreflected beam in Figure 29 and to the sample in a clean condition in Figure 30. The FWHM of the contaminated sample is 14.47 arc sec, or an increase of [illegible].09 arc sec over the clean sample. Also, in Figure 30 there is more of the reflected energy in the wings of the curve for the contaminated sample than there has been in the previous curves for fused silica.

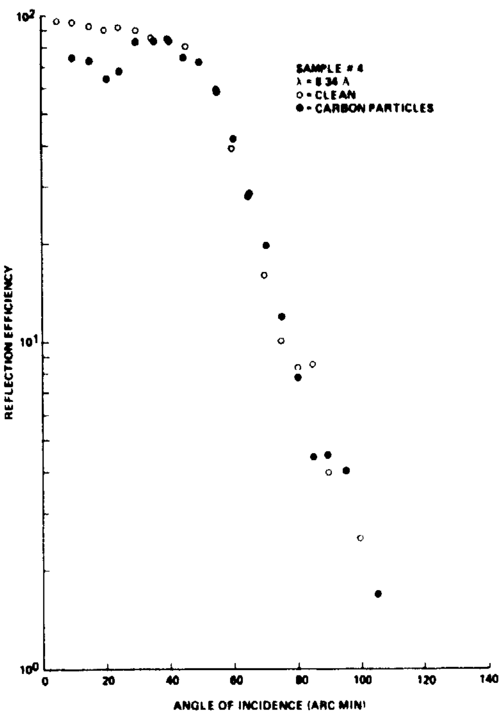

Figure 27. Reflection efficiency of clean and contaminated sample #4.

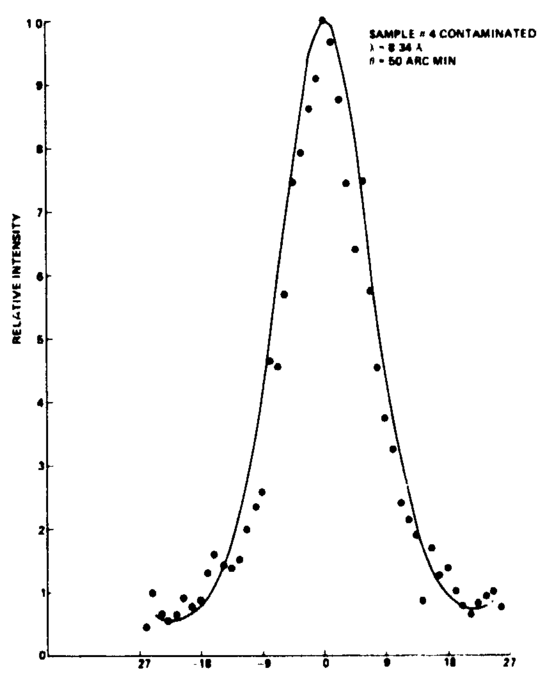

Figure 28. Fused silica sample #4 contaminated, θ = 50 arc min.

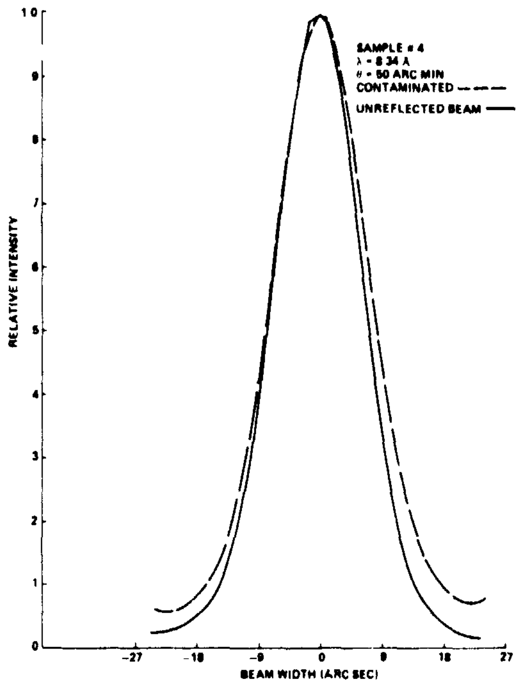

Figure 29. Comparison of contaminated sample #4 and unreflected beam.

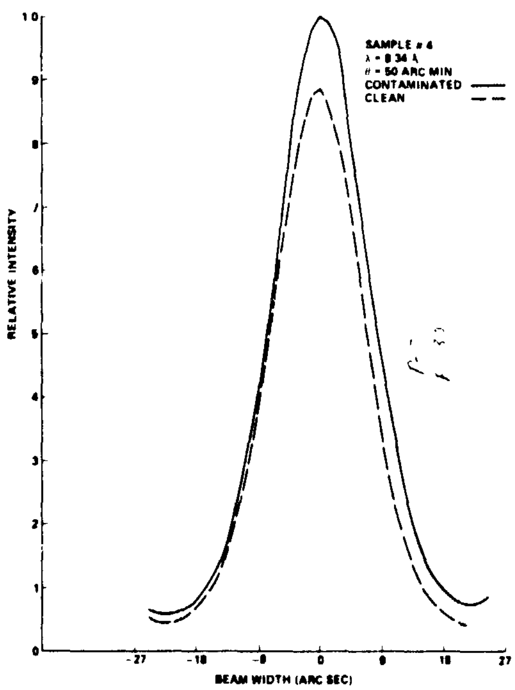

Figure 30. Sample #4 contaminated and clean, θ = 50 arc min.

5. Sample #5. This fused silica sample was cleaned, measured, contaminated with 10 μ diameter carbon particles, and then remeasured.

The experimental reflection efficiency curve for the clean sample is given in Figure 31 together with the theoretical curve. The scatter curve at θ = 50 arc min is shown in Figure 32 and is compared with the unreflected beam in Figure 33. The angular widths of the two curves at the FWHM are very similar.

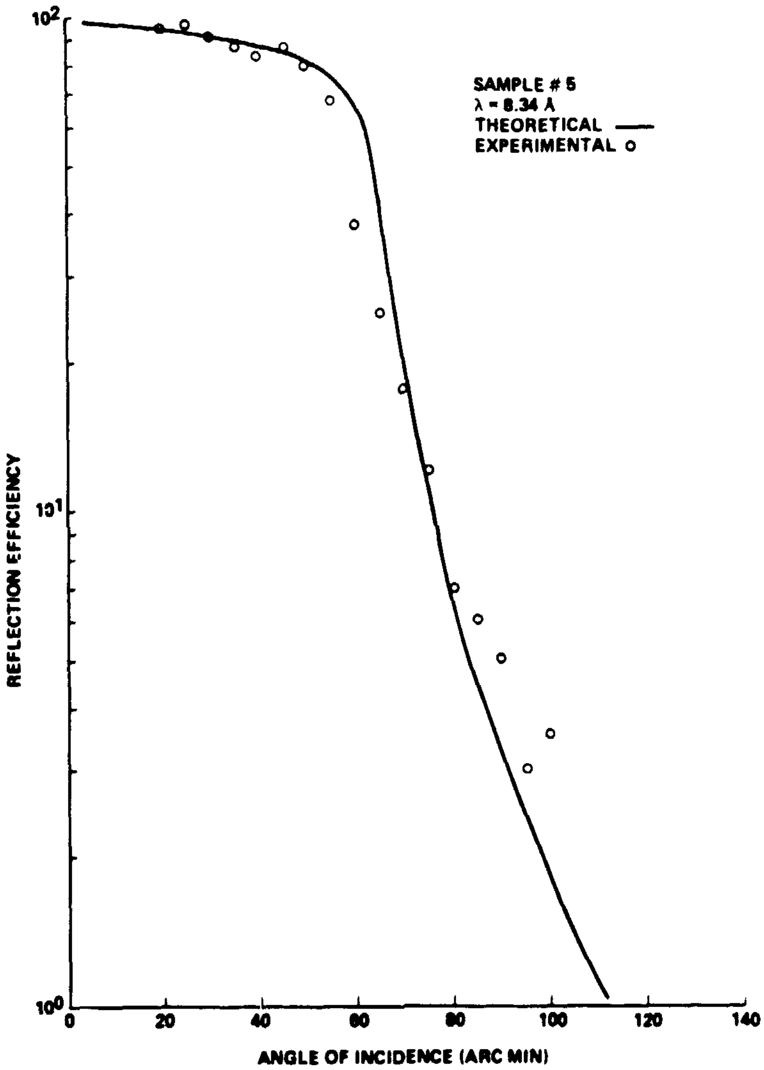

Figure 31. Reflection efficiency for fused silica sample #5.

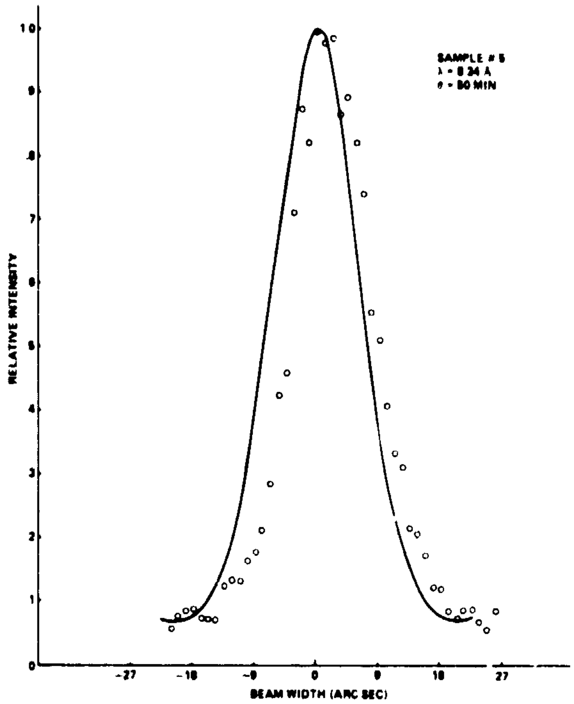

Figure 32. Fused silica sample #5, θ = 50 arc min.

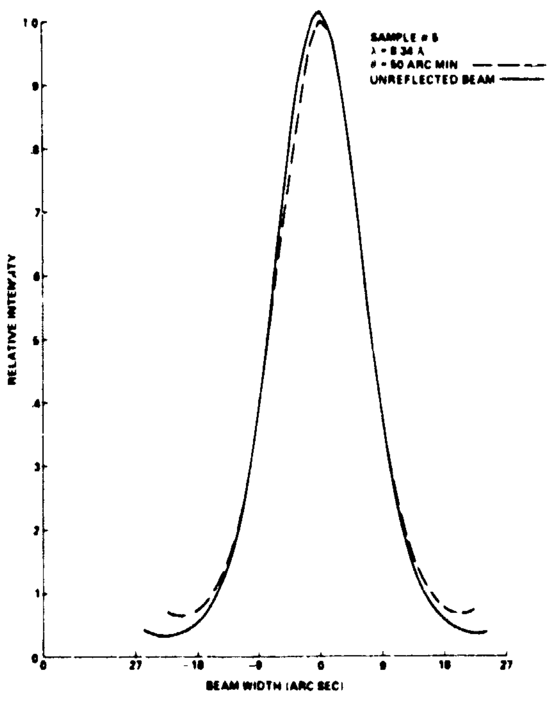

Figure 33. Comparison of sample #5 and unreflected beam.

After the sample was measured in a clean condition, it was contaminated with carbon particles to an average density of 689 particles/mm^2. The particle size distribution is shown in Figure 34. The particles ranged in size from 1 to 35 μm in diameter, with the largest number of particles in the 8 μm range. Figure 35 is a microphotograph of the sample surface after the carbon particles were deposited.

The contaminated sample was measured together with the control sample so that the changes in the measurements due to the contaminant could be isolated. Figure 36 is a plot of the reflection efficiency as a function of angle of incidence,

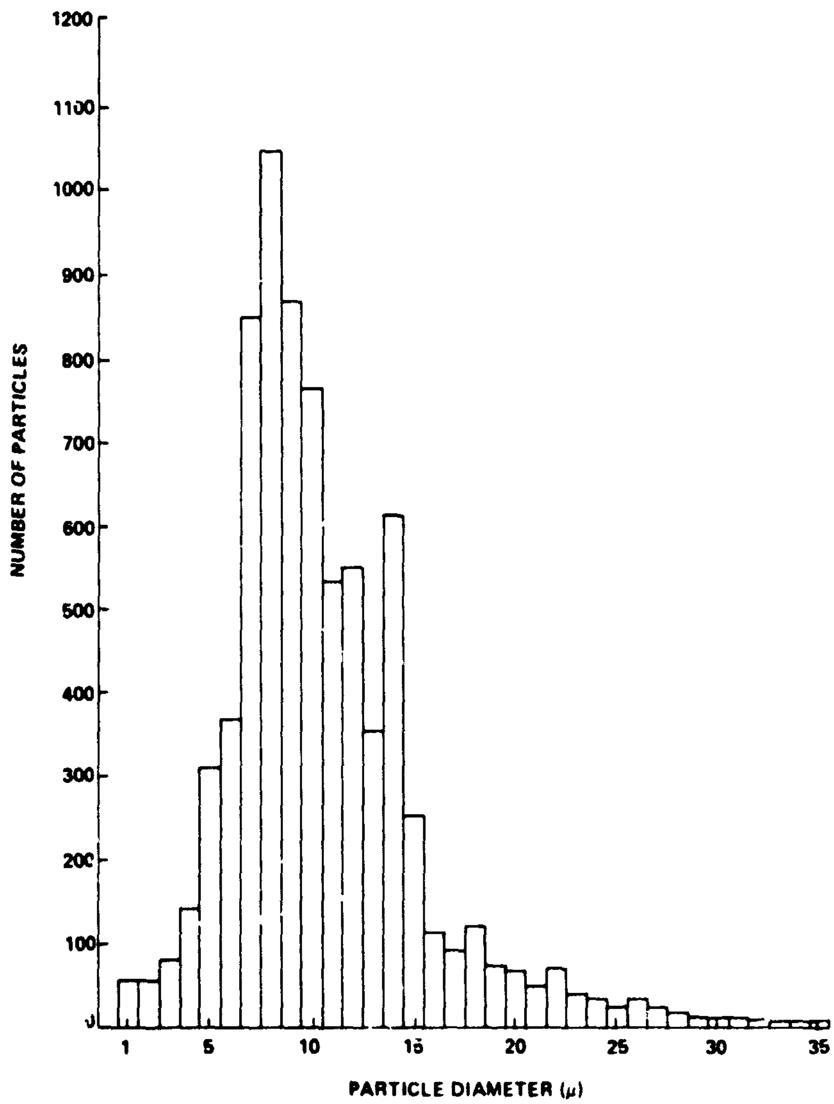

Figure 34. Size distribution of carbon particles on sample #5.

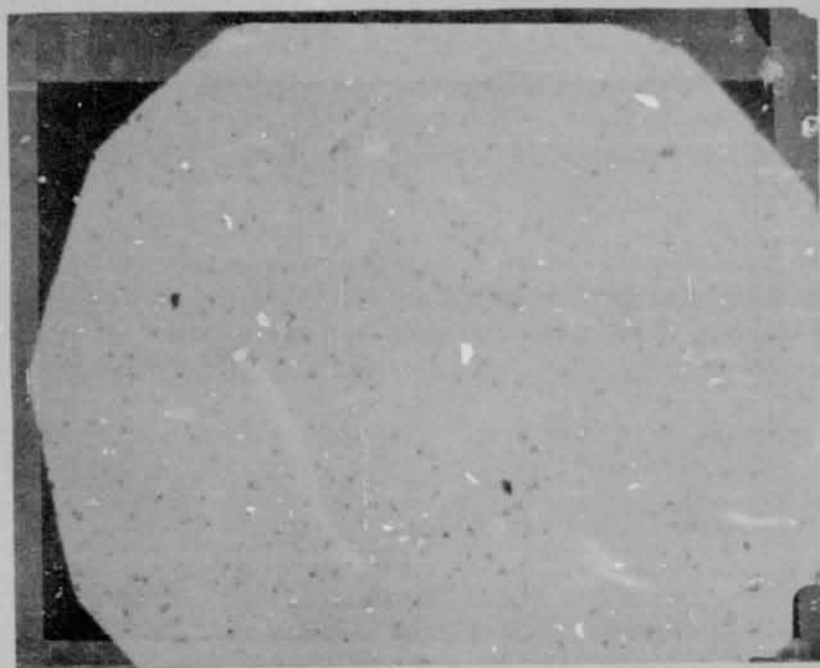

Figure 35. Sample #5 after depositing carbon particles.

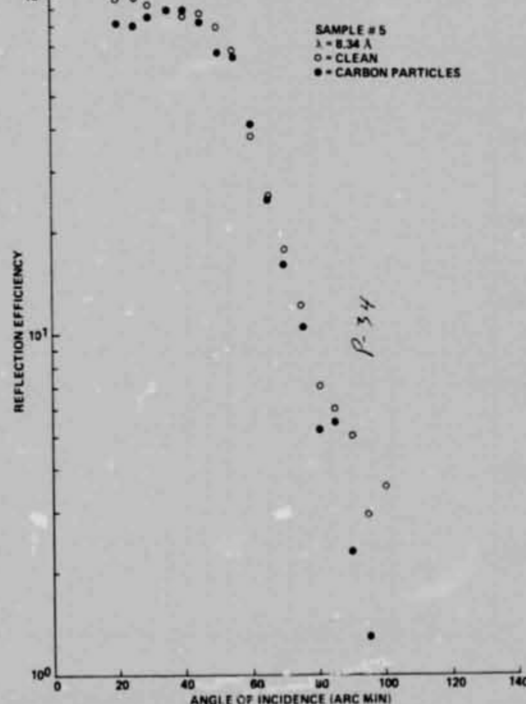

Figure 36. Reflection efficiency of clean and contaminated sample #5.

corrected to indicate changes due to the contamination. Also shown is the reflection curve for the sample prior to contamination. The effect of the carbon particles is greatest at the lowest angles of incidence, causing a decrease in the efficiency of approximately 17 percent at $\theta = 25$ arc min. At values of θ greater than the critical angle, the particles did not cause any significant reduction in the efficiency of the sample. The scatter curve for the contaminated sample is given in Figure 37 for $\theta = 50$ arc min. The FWHM is 16.88 arc sec, or an

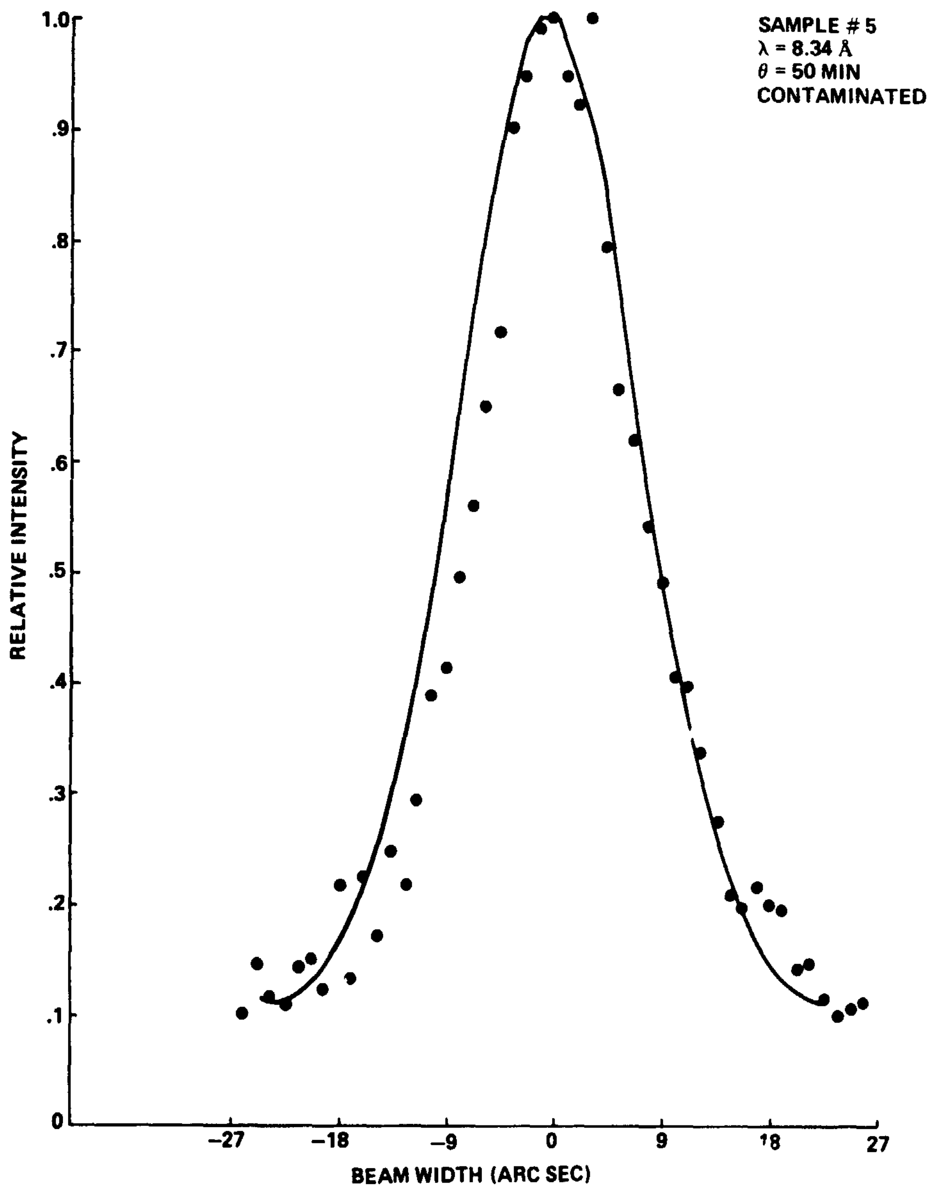

Figure 37. Fused silica sample #5 contaminated, θ = 50 arc min.

increase of 3.96 arc sec in the unreflected beam shown superimposed on the contaminated curve in Figure 38. Note that the wings of the contaminated curve contain a large portion of the total energy as compared to the wings of the unreflected curve. The scatter curve of the sample in a clean and contaminated condition are compared in Figure 39. The FWHM of the scatter curve increased by 3.27 arc sec on the contaminated sample, with the wings containing a larger portion of the total energy.

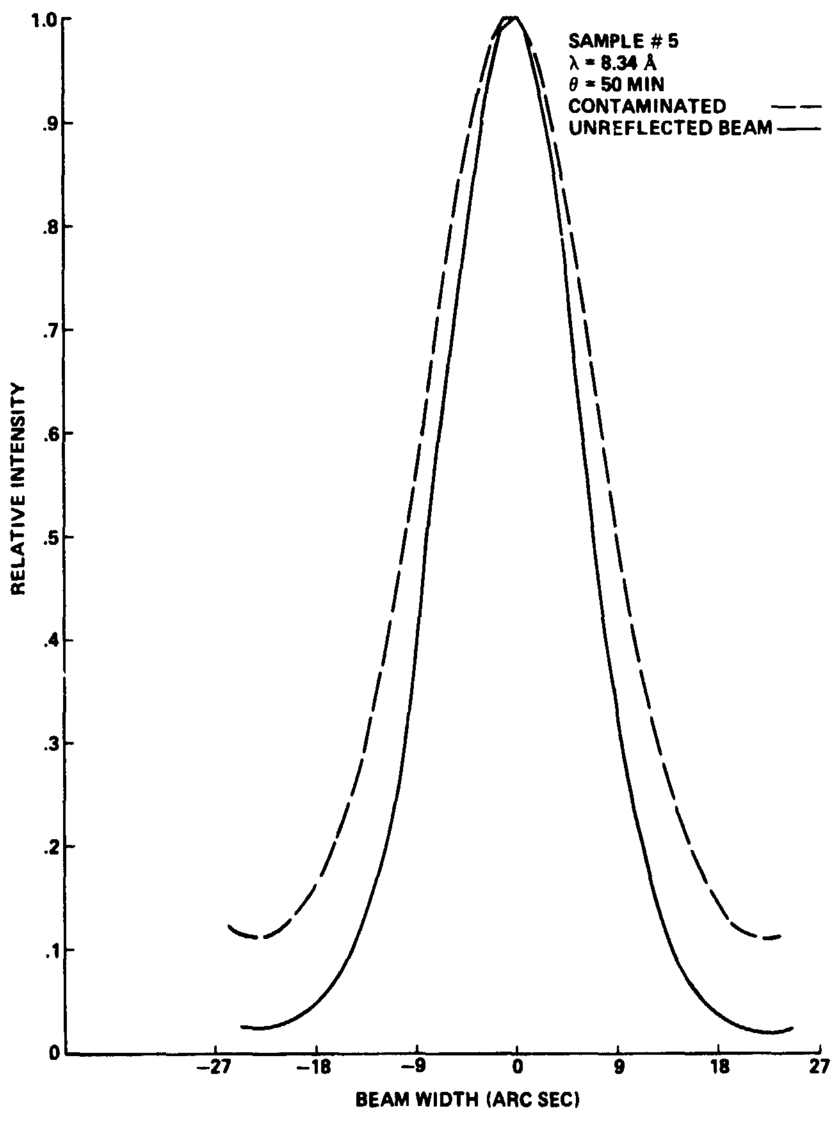

Figure 38. Comparison of contaminated sample #5 and unreflected beam.

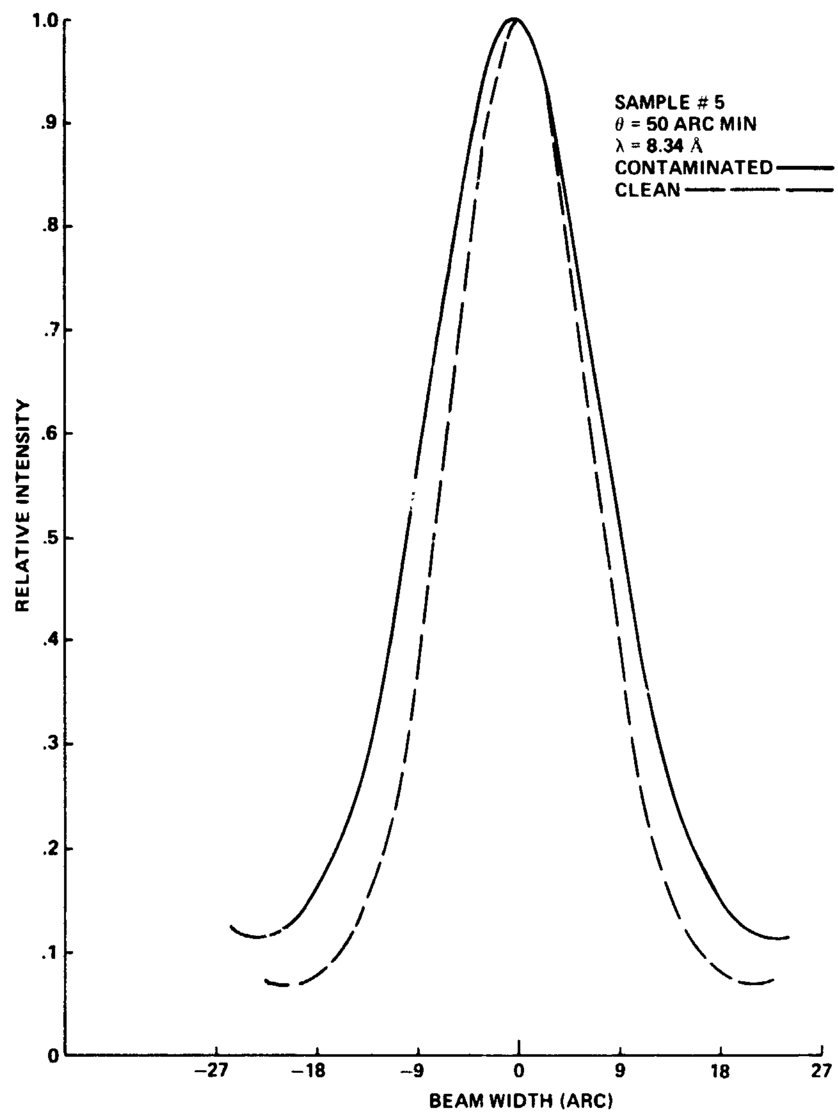

Figure 39. Sample #5 contaminated and clean, θ = 50 arc min.

Samples #4 and #5 were contaminated with 10 μm diameter carbon particles. Sample #5 contained a particle density more than six times the particle density of sample #4. The scatter curves for θ = 50 arc min are compared in Figure 40. The angular width of the curve at the FWHM for the highest density of particles is 2.41 arc sec greater than the lower density sample. The reflection efficiency of the two contaminated samples was very similar at values of θ greater than 30 arc min (Fig. 41). However, at smaller values of θ the efficiency of the sample with the lower density of particles was significantly less.

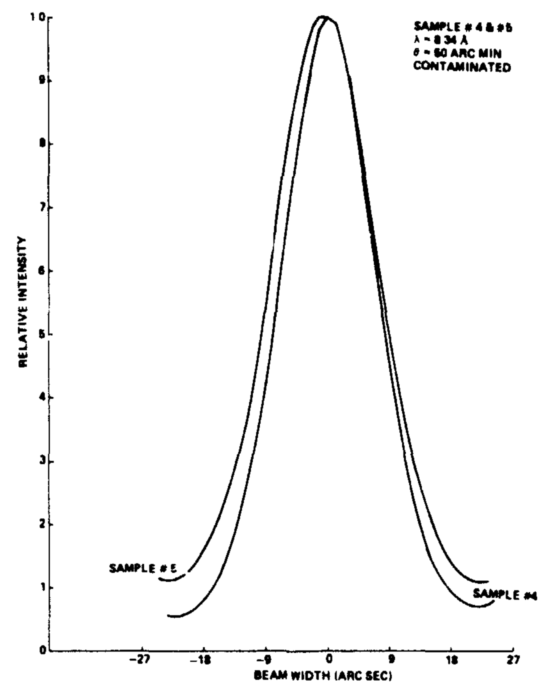

Figure 40. Comparison of contaminated samples #4 and #5, θ = 50 arc min.

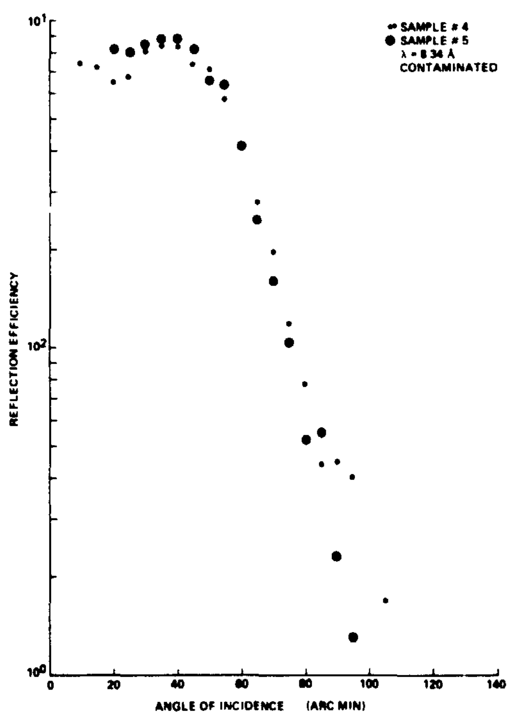

Figure 41. Reflection efficiency of contaminated samples #4 and #5.

B. Chromium

The chromium samples were prepared by depositing 1000 Å ± 25 Å of 99.999 percent purity chromium on a fused silica substrate finished to a flatness of $\lambda/10$.

1. Sample #6. The reflection efficiency of this sample was measured and is compared to the theoretical curve in Figure 42. Even though there is some spreading in the experimental data, the agreement with the theoretical data is reasonable. The theoretical curve for fused silica, the substrate material is also shown in Figure 42.

This sample was measured at several values of θ to study the angular spread in the x-ray beam as a function of the angle of incidence. The curves are presented for measurements made at angles of incidence of $\theta = 0$, 20, 40, 85, and 110 arc min in Figures 43 through 47. The curve for the unreflected beam is given in Figure 48.

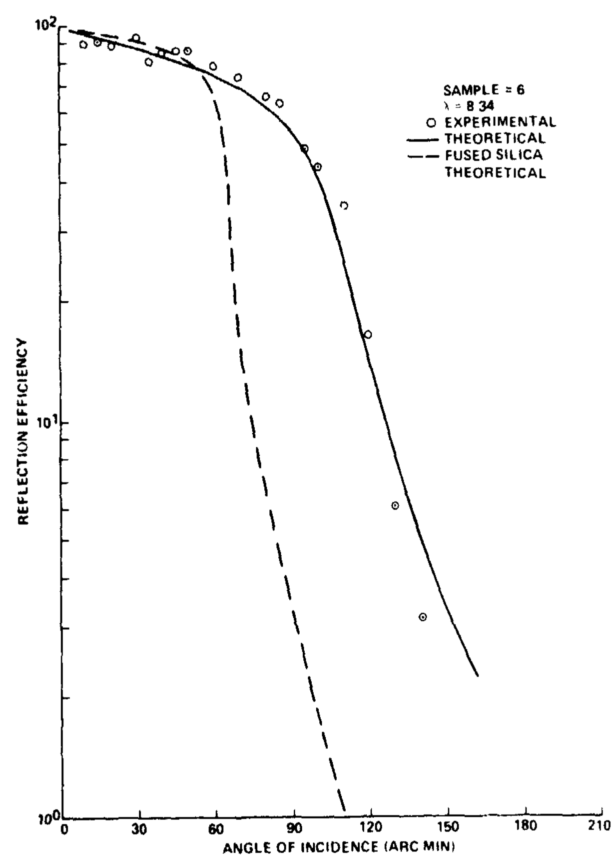

Figure 42. Reflection efficiency for chromium sample #6.

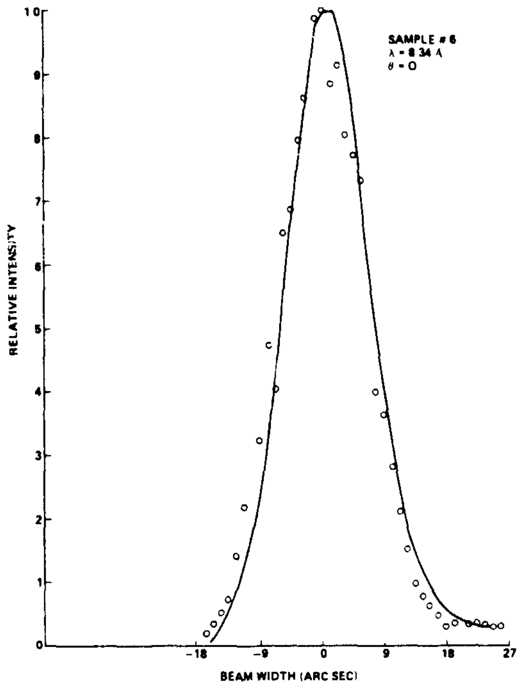

Figure 43. Chromium sample #6, $\theta = 0$.

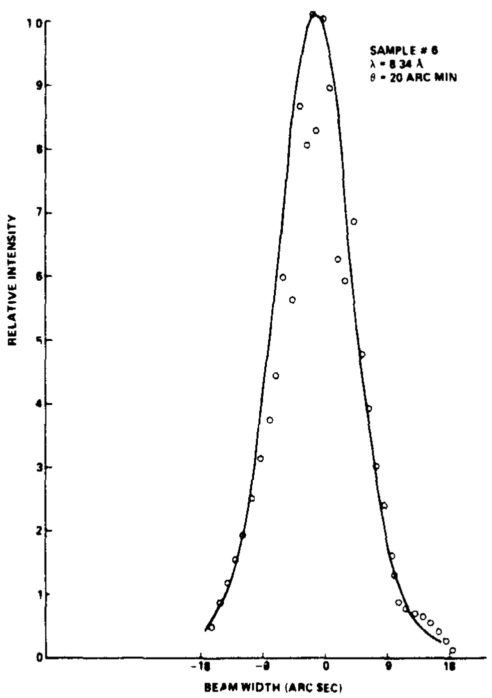

Figure 44. Chromium sample #6, $\theta = 20$ arc min.

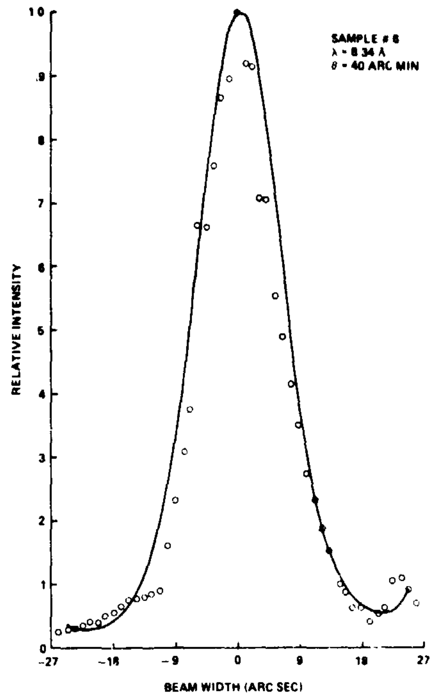

Figure 45. Chromium sample #6, θ = 40 arc min.

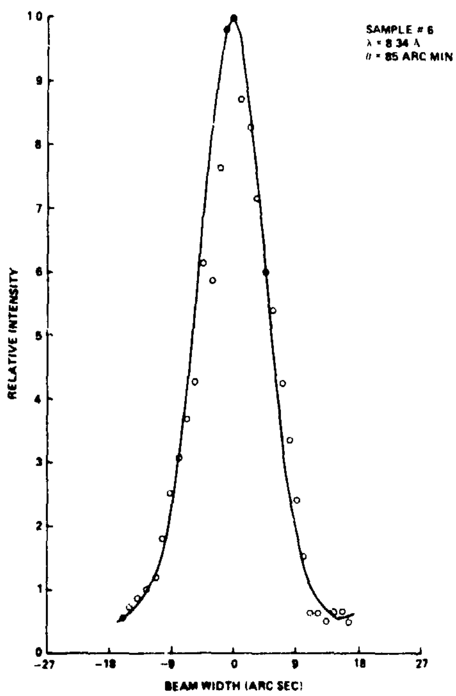

Figure 46. Chromium sample #6, θ = 85 arc min.

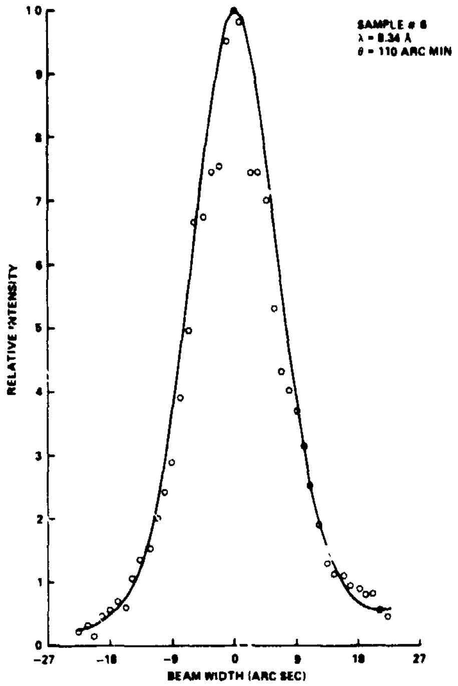

Figure 47. Chromium sample #6, θ = 110 arc min.

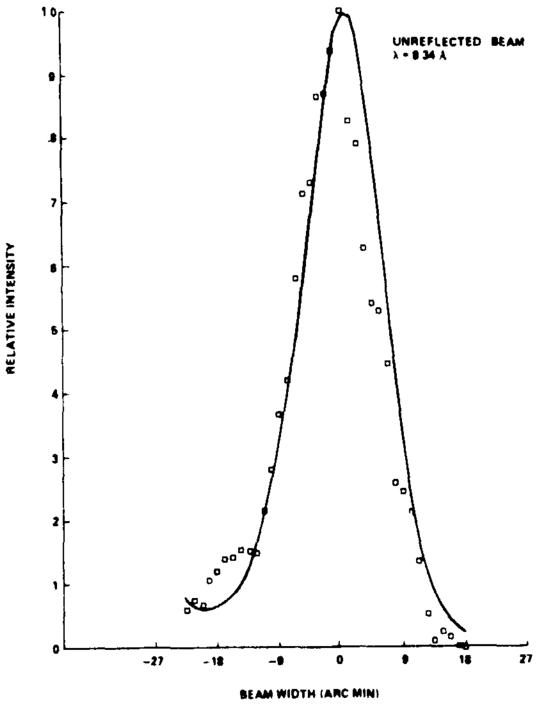

Figure 48. Unreflected x-ray beam for sample #6.

After the aforementioned measurements were completed, the sample was removed from the x-ray reflectometer and placed in the contamination chamber shown schematically in Figure 49. The sample was exposed to Skylab thermal control material S13-G, a white paint with a potassium silicate treated zinc oxide pigment placed in a polydimethyl-siloxane binder [5]. Sample #6 was exposed to the vacuum environment for 24 hours during which time the temperature of the thermal control sample (S13-G) was maintained at 55°C. The chromium sample was maintained at 20°C and the vacuum chamber at 35°C. Due to the pumping action of the system and the thermodynamic parameters established, all outgassed products will pass by the chromium sample and condense on its face. Following this exposure, the sample was placed in the x-ray reflectometer and remeasured. The reflection efficiency curve is given in Figure 50 and compared to the reflection efficiency curve prior to exposure to the S13-G paint in Figure 51. The contamination reduced the reflection efficiency of the sample by approximately 20 percent at angles of incidence less than the critical angle, and at values of θ greater than the critical angle, the efficiency appears to be as great as the uncontaminated sample.

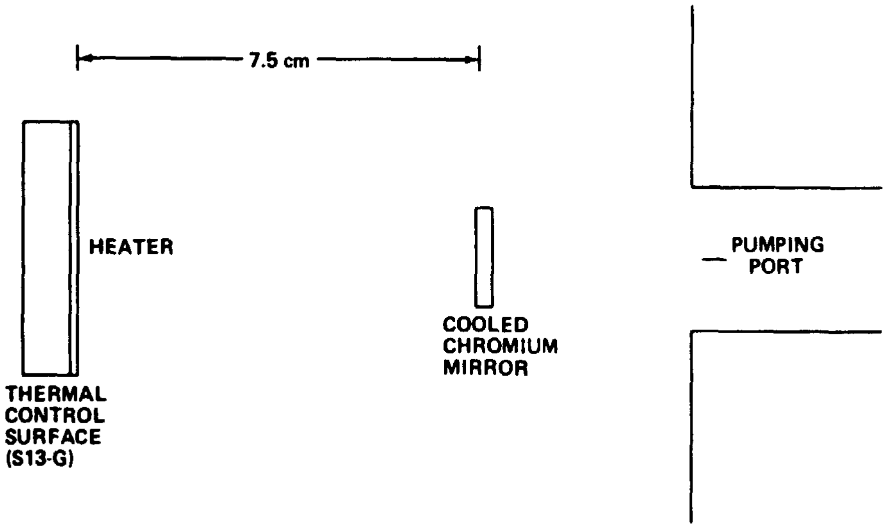

Figure 49. Schematic of contamination chamber.

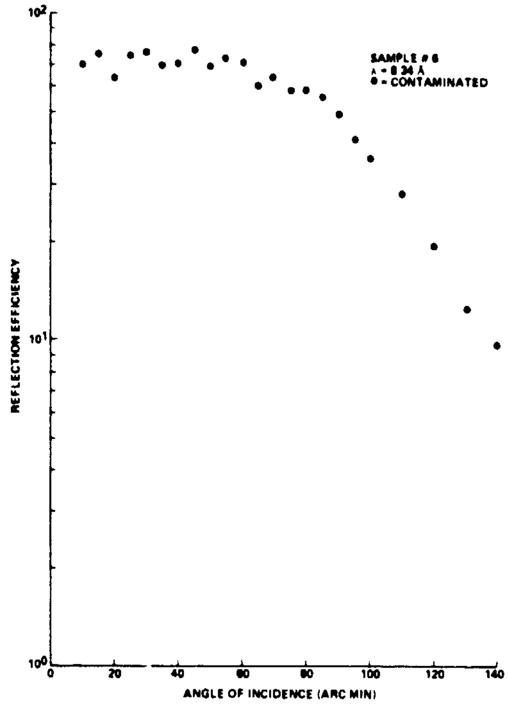

Figure 50. Reflection efficiency of contaminated sample #6.

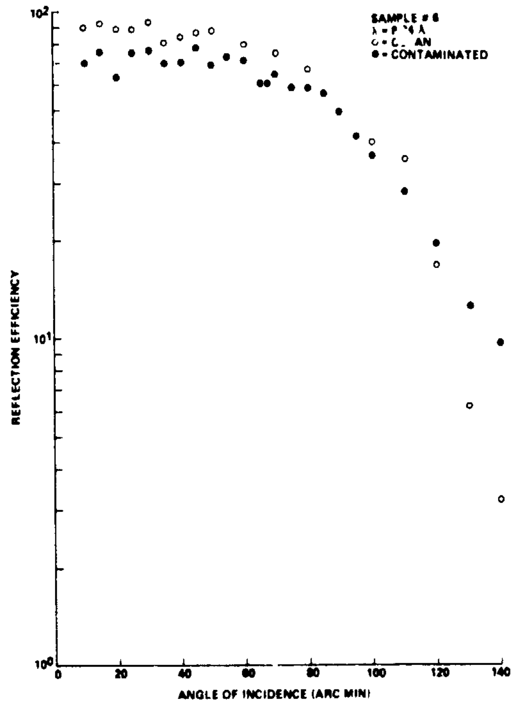

Figure 51. Reflection efficiency of clean and contaminated sample #6.

The scatter curves for the sample after exposure to S13-G for the same values of θ are given in Figures 52 through 56 and are compared to the clean sample in Figures 57 through 61. The angular change in the FWHM between the clean sample and the contaminated sample is given in Figure 62 as a function of the angle of incidence θ. The angular width at the FWHM of the contaminated sample increased for all values of θ except $\theta = 0$. With the alignment technique used with the x-ray reflectometer this would be expected if a material were deposited onto the sample. Although the FWHM did increase for all values of θ greater than zero, there did not appear to be a trend in the data.

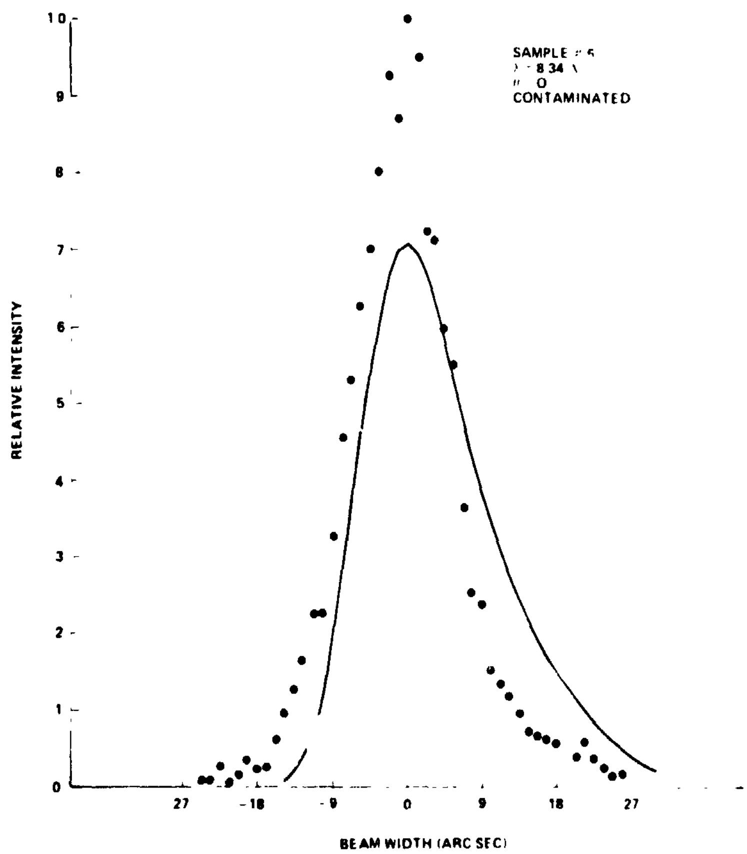

Figure 52. Chromium sample #6 contaminated, $\theta = 0$.

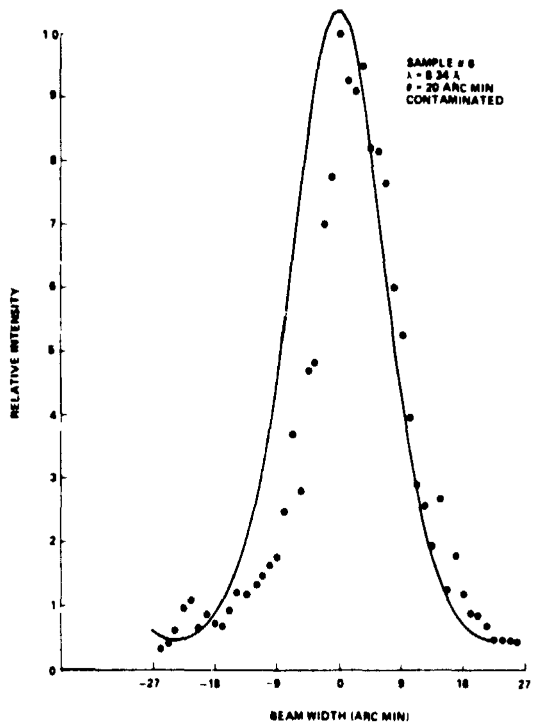

Figure 53. Chromium sample #6 contaminated, θ = 20 arc min.

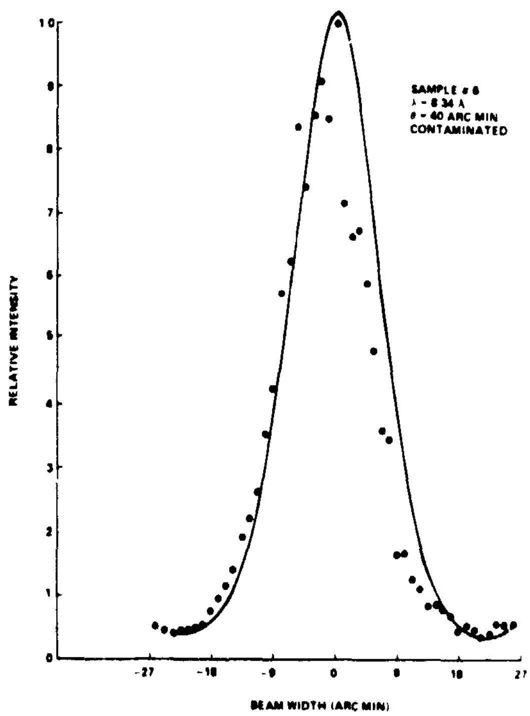

Figure 54. Chromium sample #6 contaminated, θ = 40 arc min.

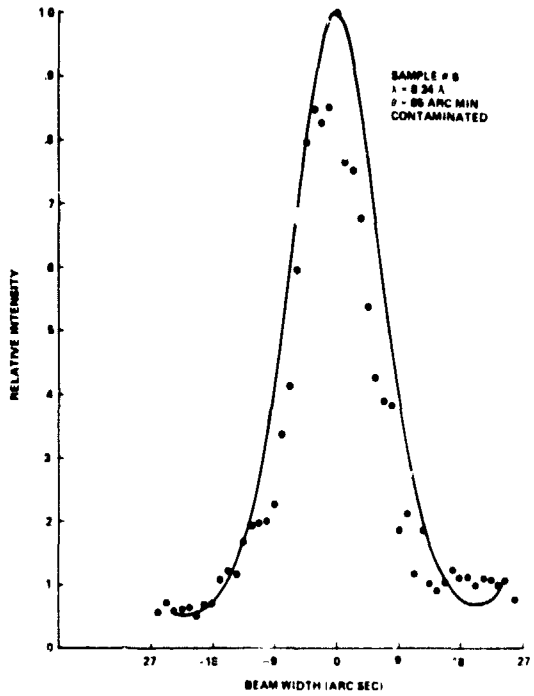

Figure 55. Chromium sample #6 contaminated, θ = 85 arc min.

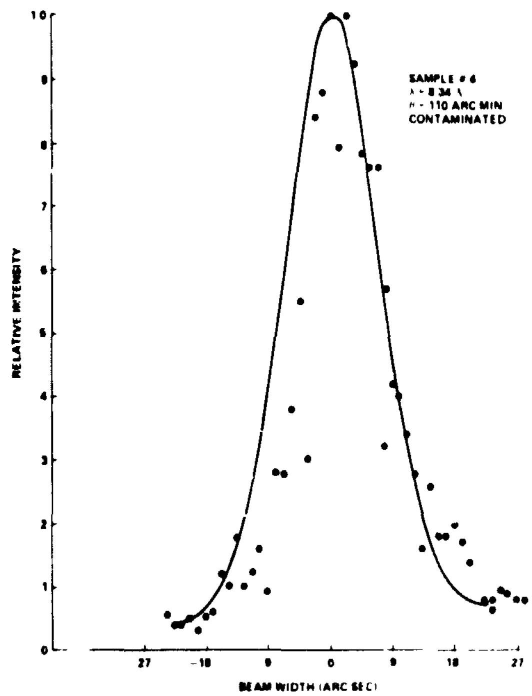

Figure 56. Chromium sample #6 contaminated, θ = 110 arc min.

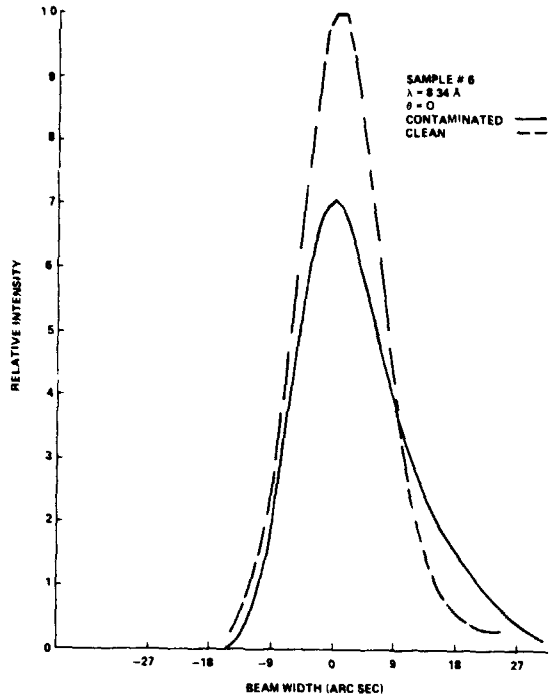

Figure 57. Sample #6 contaminated and clean, $\theta = 0$.

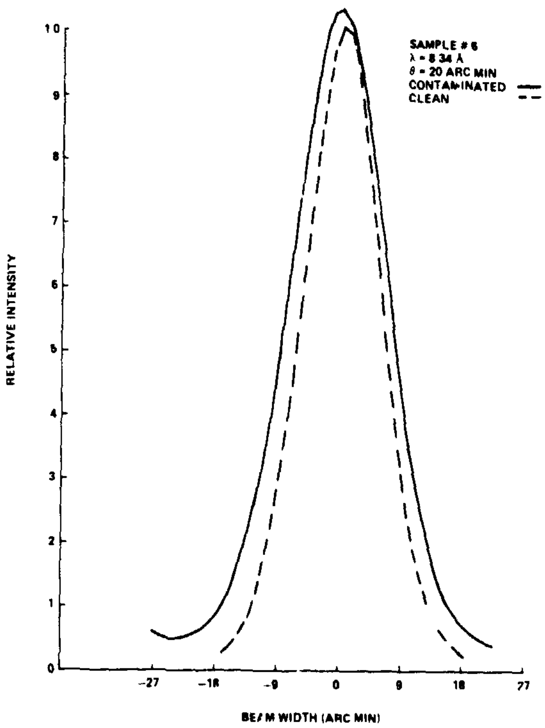

Figure 58. Sample #6 contaminated and clean, θ = 20 arc min.

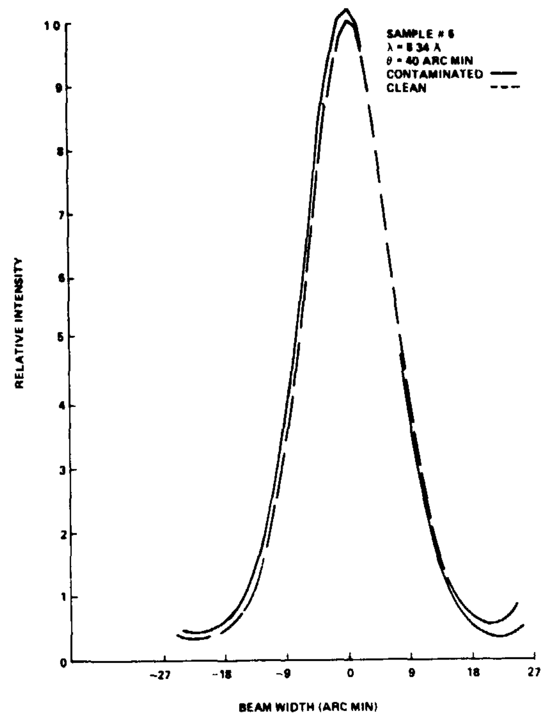

Figure 59. Sample #6 contaminated and clean, $\theta = 40$ arc min.

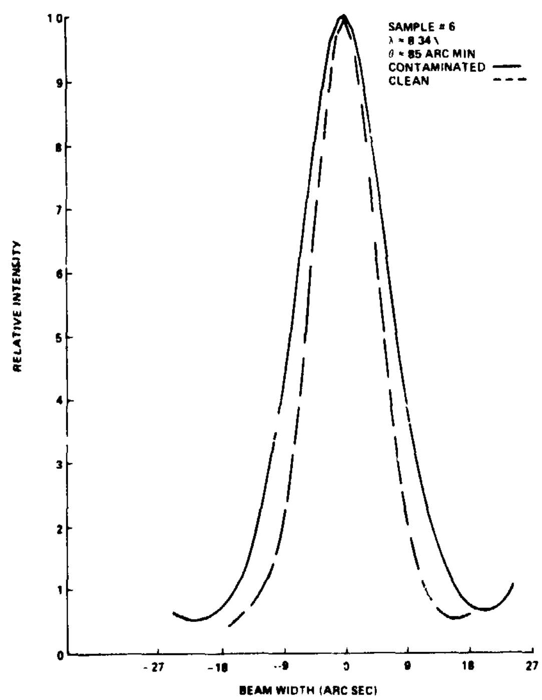

Figure 60. Sample #6 contaminated and clean, $\theta = 85$ arc min.

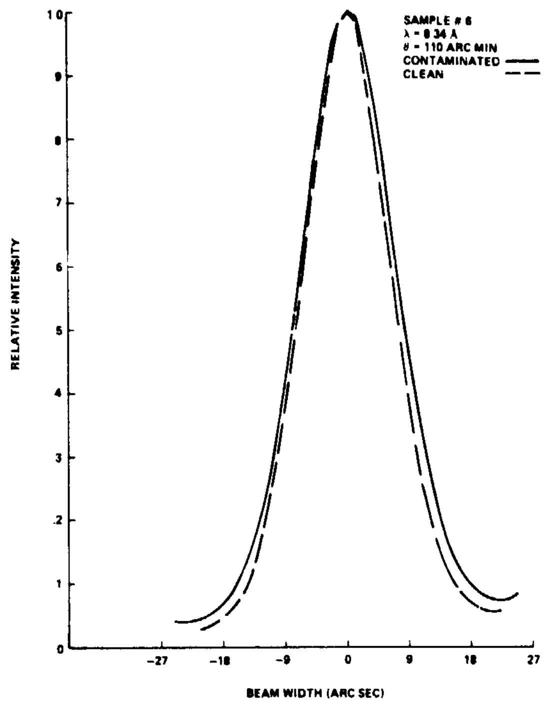

Figure 61. Sample #6 contaminated and clean, θ = 110 arc min.

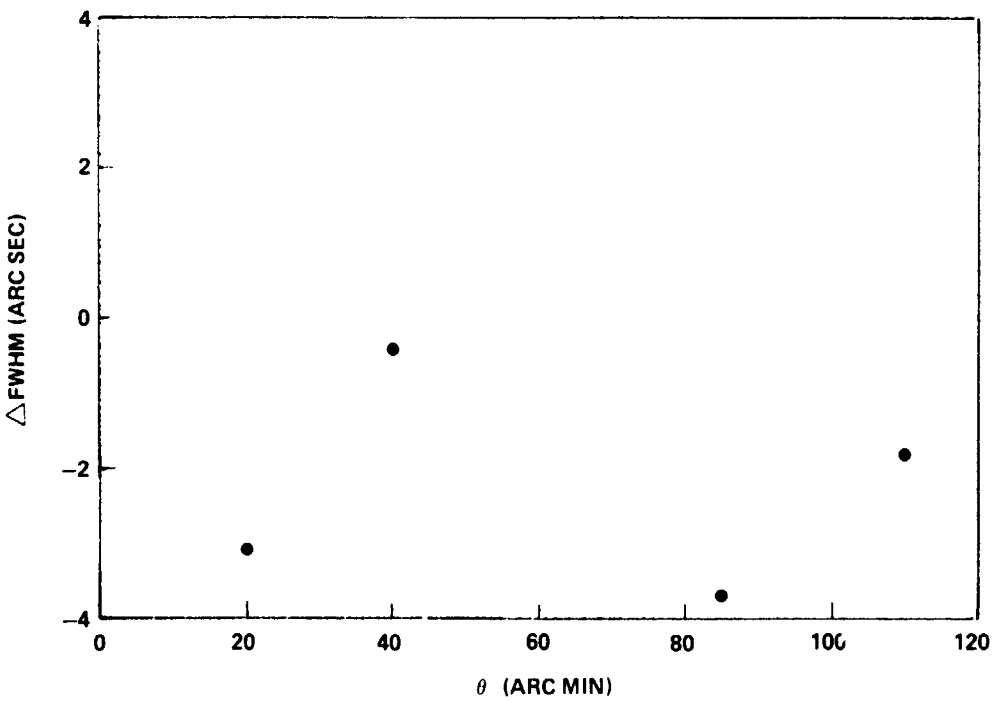

Figure 62. Difference in the FWHM of clean and contaminated sample #6.

2. Sample #7. This sample was cleaned and placed on top of a storage cabinet in a warehouse for 48 hours and allowed to collect dust. The sample was removed and a particle count taken. The particle density was 9 particles/mm^2, with the largest number of particles in the 5 to 10 μm range. A histogram of the particle count is given in Figure 63, with the particle size ranging from 5 to 30 μm in diameter. The sample was then placed in the reflectometer and measured to determine the reflection efficiency and scatter parameters. The reflection efficiency is given in Figure 64 and the scatter curve in Figure 65. The sample was not measured in a clean condition and therefore has to be

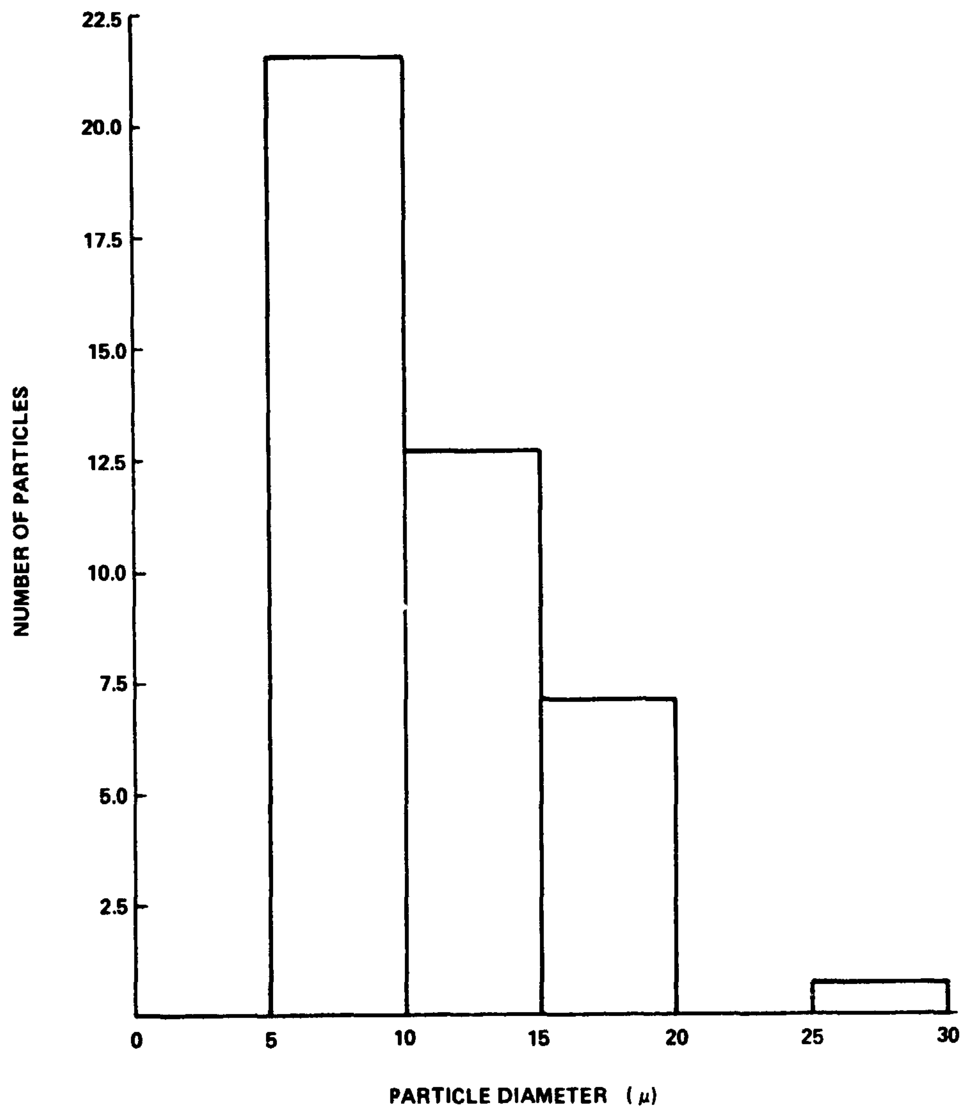

Figure 63. Size distribution of dust particles on sample #7.

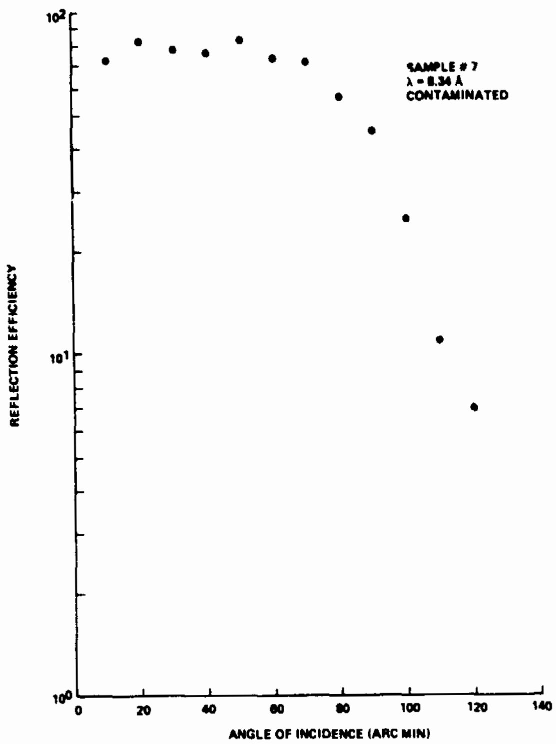

Figure 64. Reflection efficiency of contaminated sample #7.

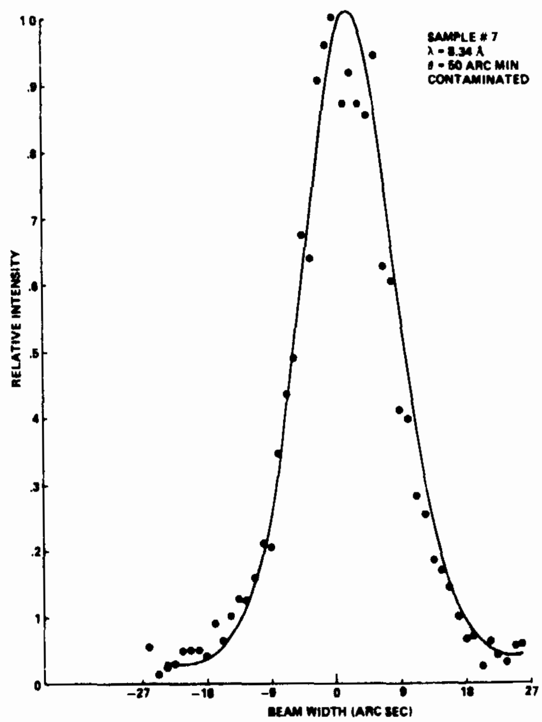

Figure 65. Chromium sample #7 contaminated, θ = 50 arc min.

compared to a sample previously tested. The reflection efficiency curve is compared to a clean sample in Figure 66. At values of θ less than 50 arc min the efficiency of the contaminated sample is slightly less than for a clean sample of the same material. The FWHM of the dust sample was 13.17 arc sec, an increase of 0.71 arc sec over the clean sample (Fig. 67). The scatter curve is compared to the unreflected beam in Figure 68.

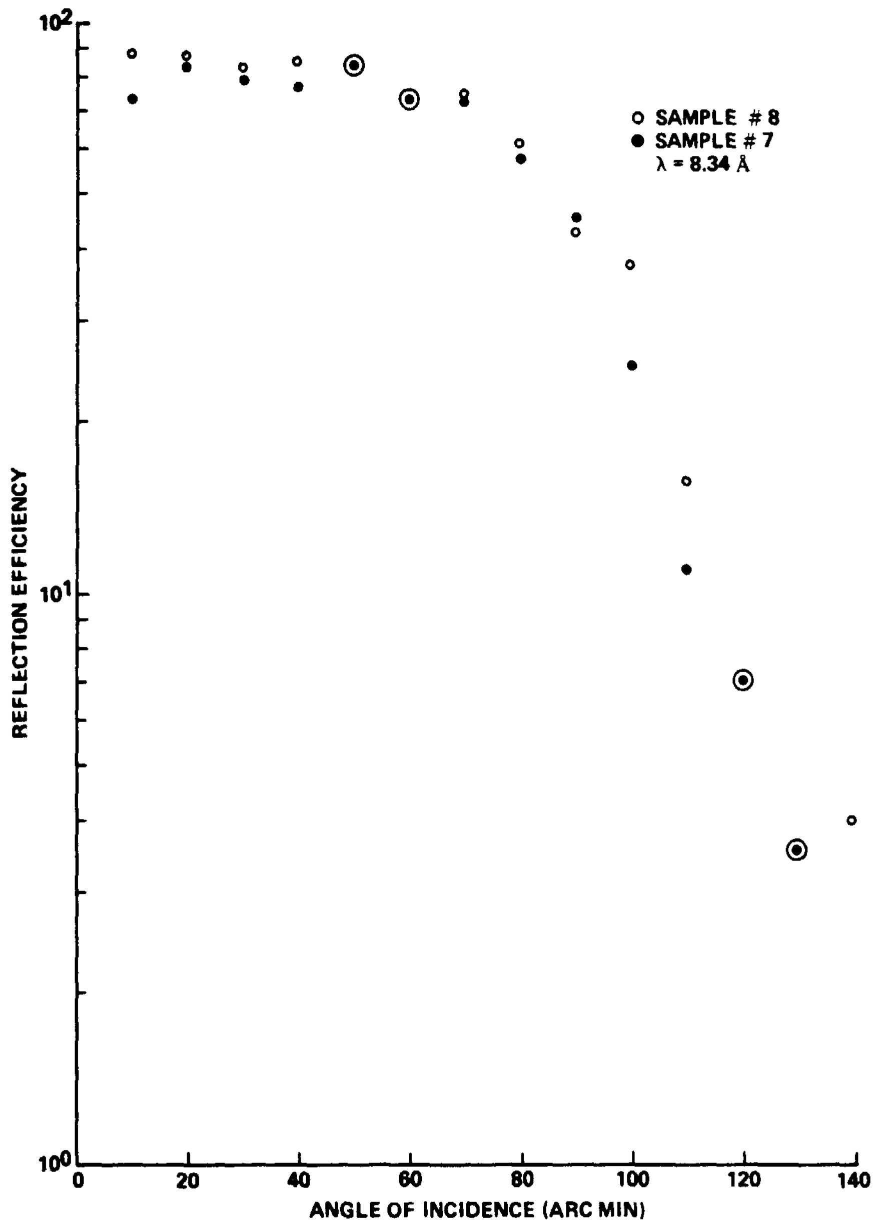

Figure 66. Reflection efficiency of clean and contaminated chromium samples.

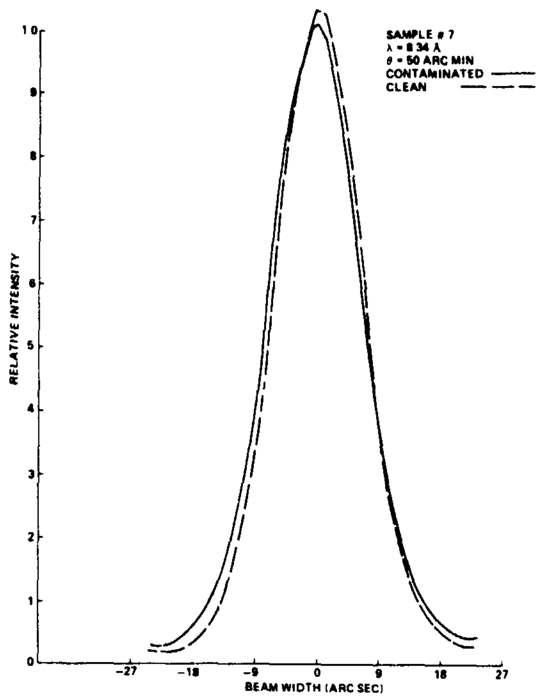

Figure 67. Comparison of contaminated and clean chromium samples, θ = 50 arc min.

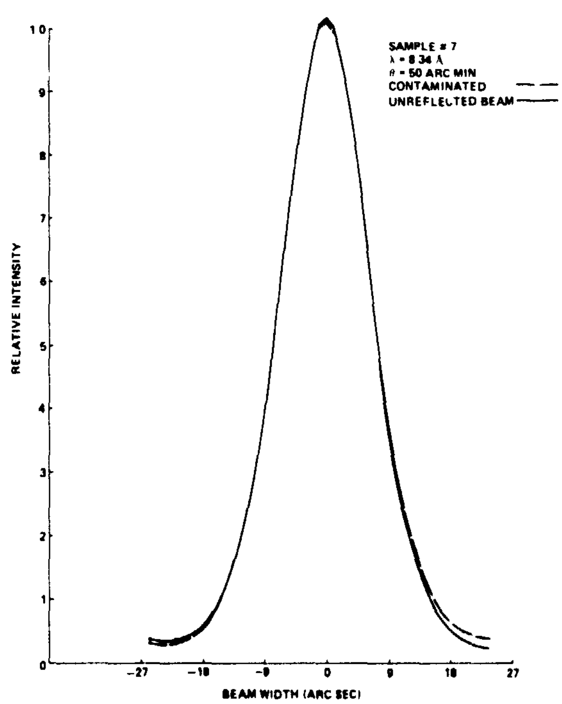

Figure 68. Comparison of contaminated sample #7 and unreflected beam.

3. <u>Sample #8</u>. This sample was measured in a clean and contaminated condition. The measured and theoretical reflection efficiency curves for the clean sample are given in Figure 69 and show reasonably good agreement between the two. After the measurements on the clean sample were completed, it was contaminated by passing basalt dust through a 10 μm diameter sieve. Basalt was used because it was readily available in the lab and because it differed from the carbon and regular dust by having more rounded particles. The particle density was 235 particles/mm^2, with the largest number of particles at 14 μm diameter (Fig. 70). The contaminated sample was measured to determine the reflection efficiency (Fig. 71). The efficiency at θ = 10 arc min was

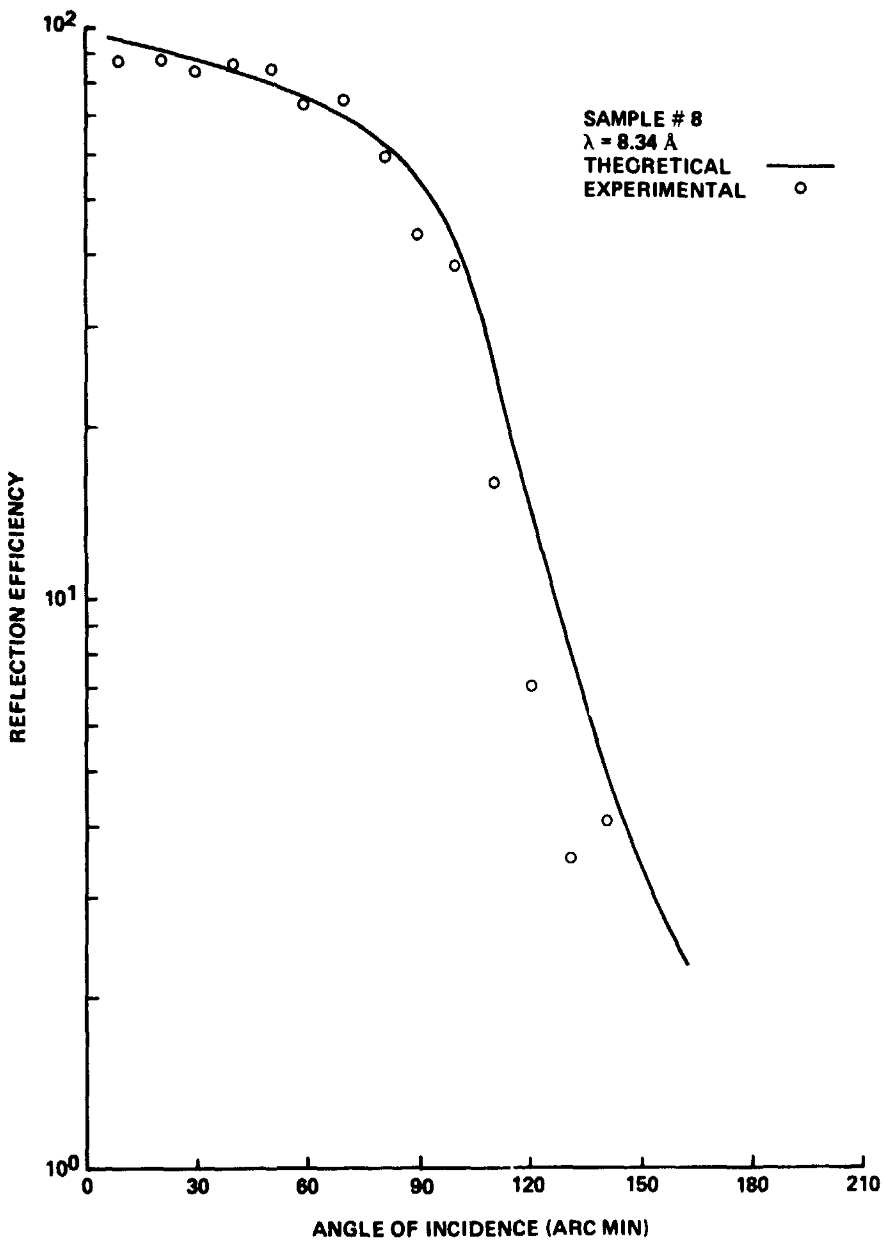

Figure 69. Reflection efficiency for chromium sample #8.

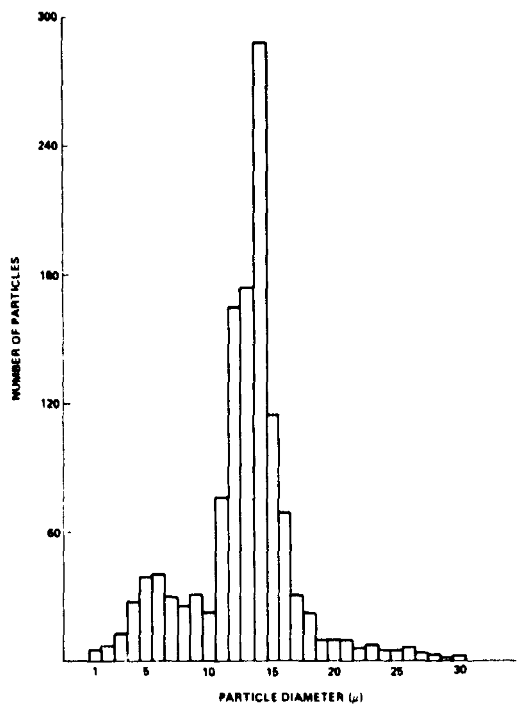

Figure 70. Size distribution of basalt particles on sample #8.

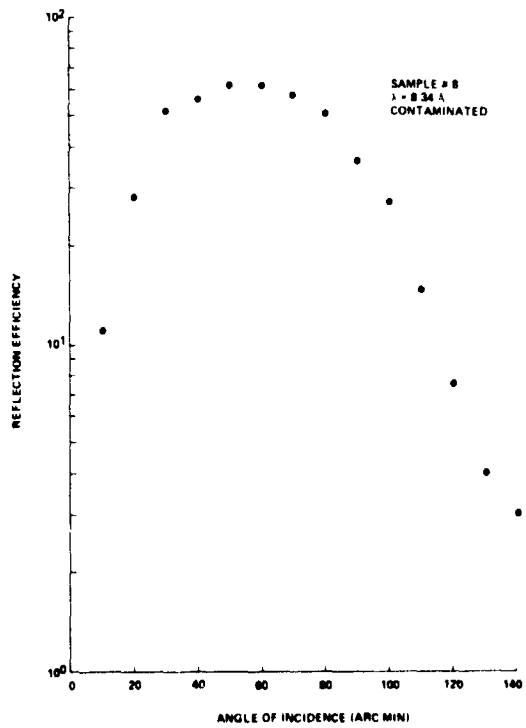

Figure 71. Reflection efficiency of contaminated sample #8.

only 11 percent, which is a reduction of 78 percent from the clean sample (Fig. 72). The efficiency of the contaminated sample increased as θ increased until the angle of incidence was 50 arc min. At this point the contaminated curve was approximately 15 percent below the clean sample. The scatter curve for the sample measured prior to depositing the particles is given in Figure 73 with a FWHM of 13.0 arc sec. It is compared to the contaminated sample in Figure 74. The FWHM of the contaminated curve is 16.57 arc sec, or an increase of 3.57 arc sec over the clean sample. The contaminated scatter curve is compared to the unreflected beam in Figure 75.

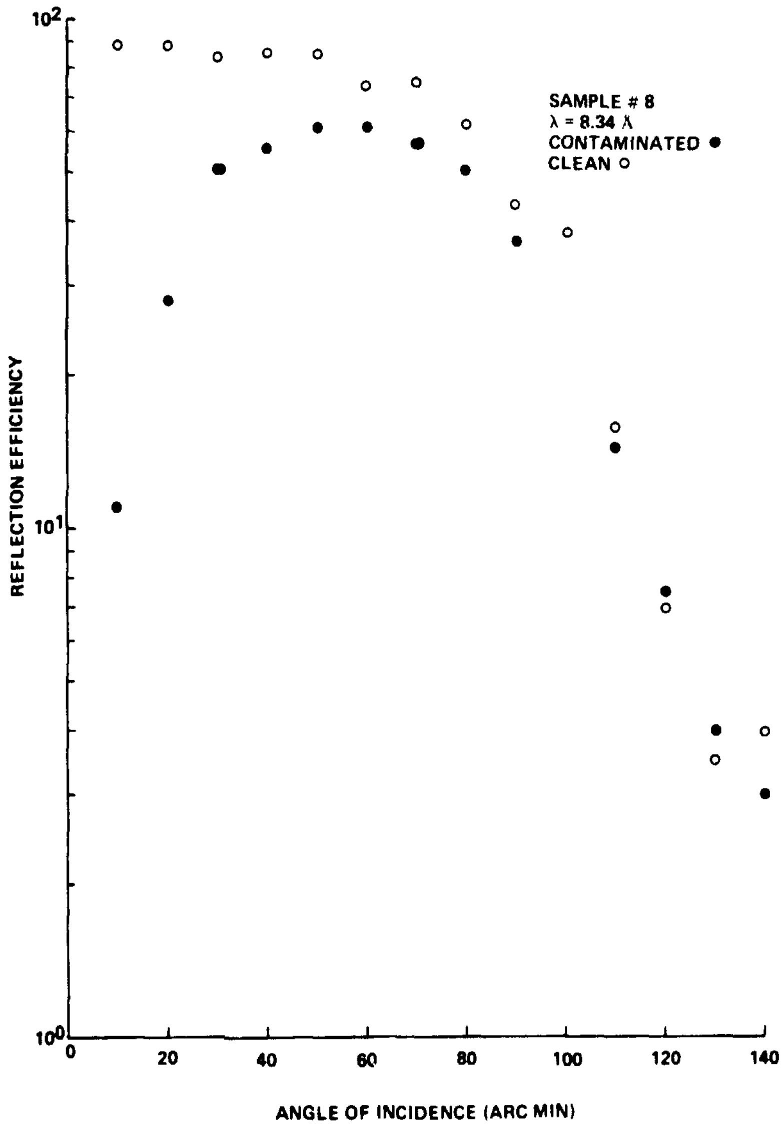

Figure 72. Reflection efficiency of clean and contaminated sample #8.

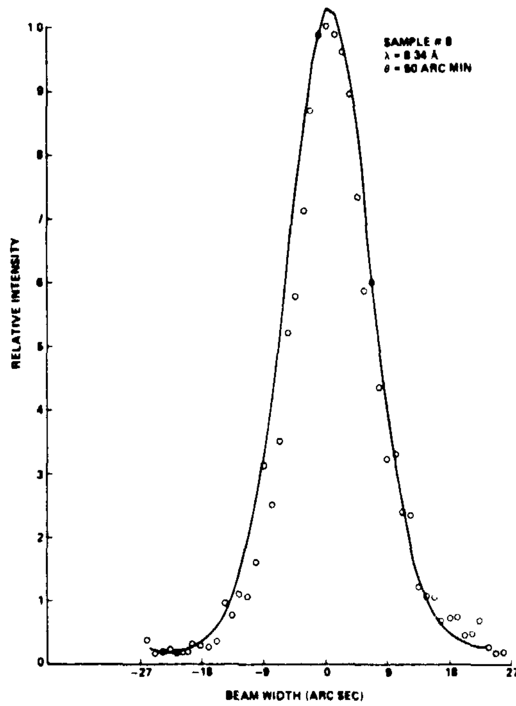

Figure 73. Chromium sample #8 contaminated, θ = 50 arc min.

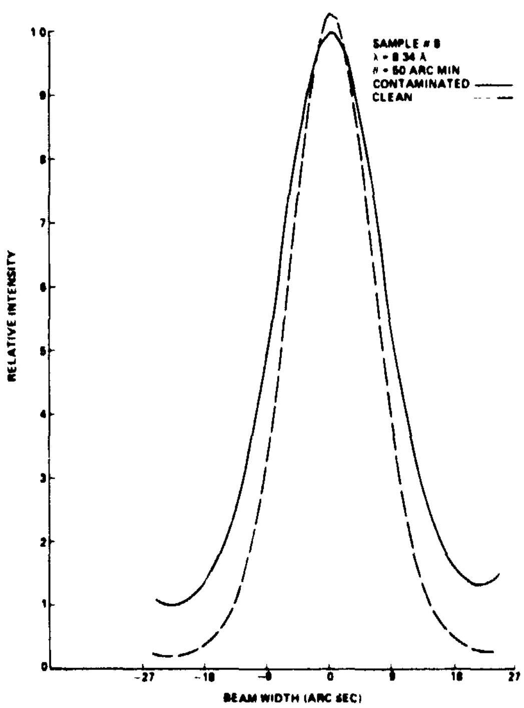

Figure 74. Sample #8 contaminated and clean, θ = 50 arc min.

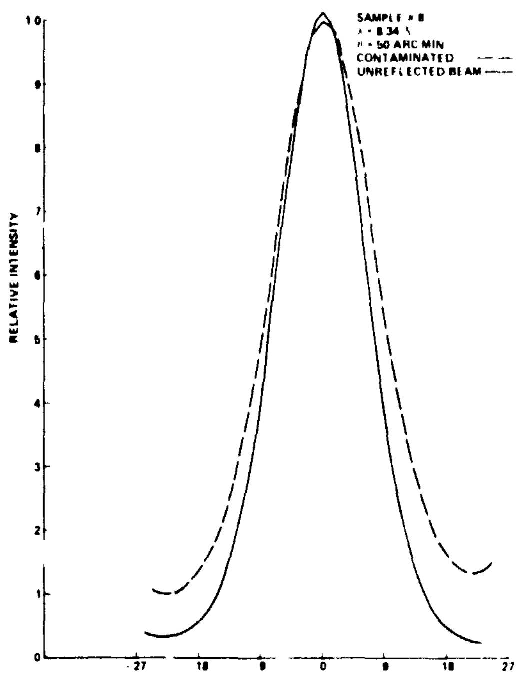

Figure 75. Comparison of contaminated sample #8 and unreflected beam.

4. Sample #9. This sample was contaminated with the same basalt material as sample #8. Because of equipment breakdown, a particle count was not made; however, the density was several times the density of the dust on sample #8. Figure 76 is a photograph of the sample. The dark areas around the edges of the sample were caused by handling the sample after the measurements were made. The reflection efficiency curve for the sample containing the particles is given in Figure 77 and is compared to the clean sample in Figure 78. At angles of incidence of 10 and 20 arc min the sample reflected the x-rays at very low efficiency, and the efficiency went to zero at θ = 30 arc min. As θ was increased, the efficiency rose to 11 percent at θ = 70 arc min and then decreased as θ increased. The intensity of the reflected x-ray beam on the contaminated sample was not sufficient to obtain a scatter curve.

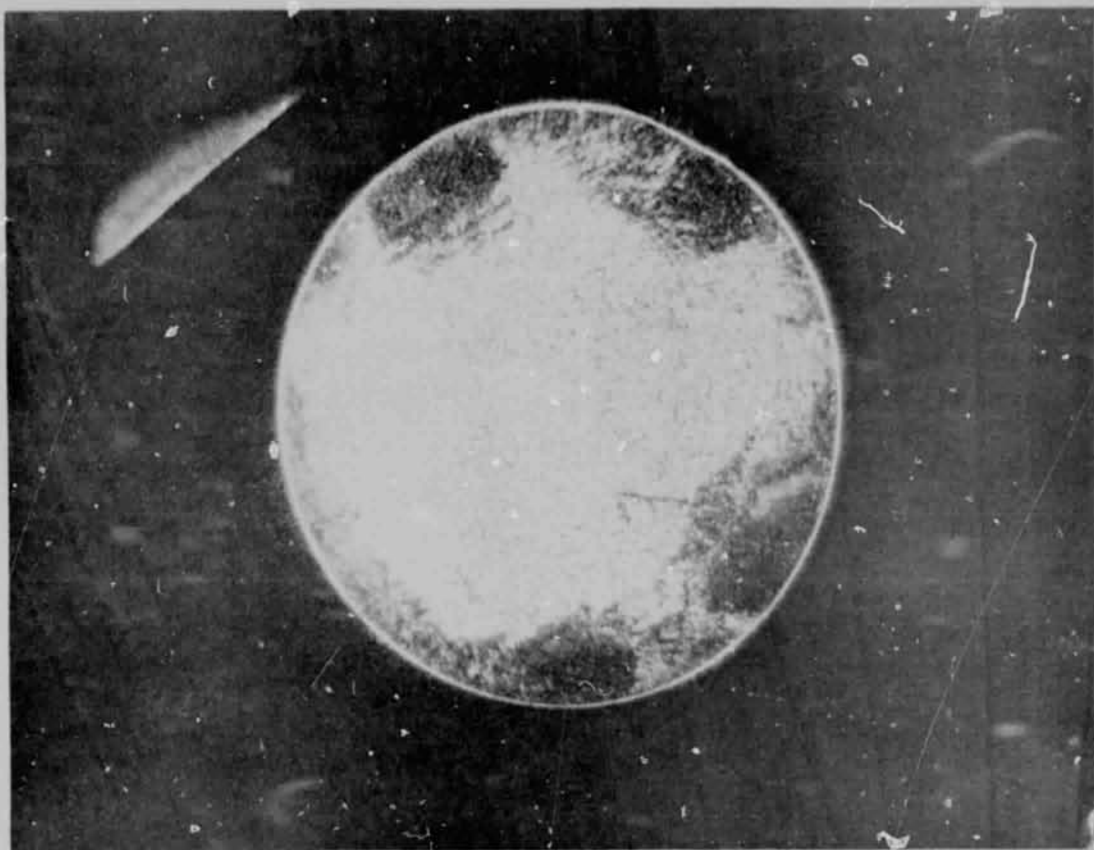

Figure 76. Sample #9 after depositing basalt particles.

V. CONCLUSIONS

These measurements were made to (1) determine the reflection efficiency of high-quality optical flats, (2) compare the results with theoretical data, (3) define the profile of the x-ray beam prior to reflecting by the sample, (4) determine how the sample scattered the x-ray beam, (5) correlate the scatter data to the reflection efficiency data, and (6) determine the effects of contamination on the reflection properties of the samples. 8.34 Å x-rays were used for all of the measurements reported, and the x-ray reflectometer was aligned such that the maximum resolution during these measurements was 12.38 arc sec.

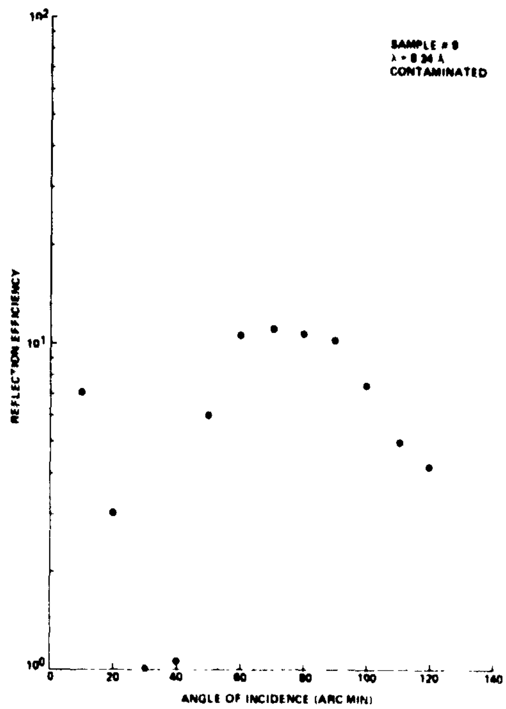

Figure 77. Reflection efficiency of contaminated sample #9.

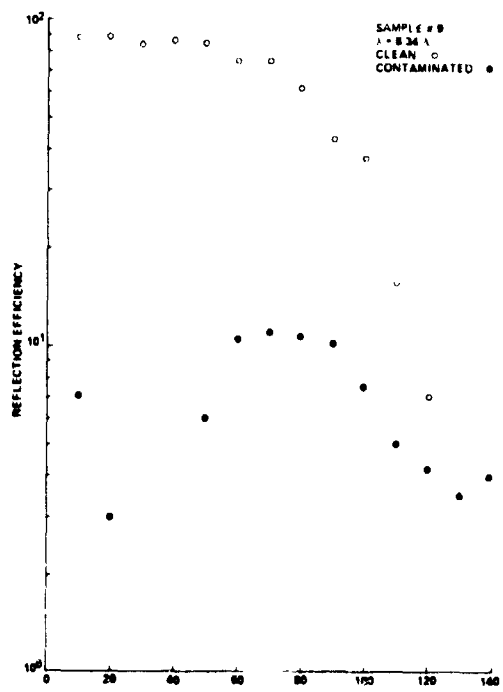

Figure 78. Reflection efficiency of clean and contaminated sample #9.

The reflection efficiency measurements on the fused silica samples compared favorable to the theoretical curves, indicating that the sample surface finish was very good. The scatter curves confirmed that the surface finish of the fused silica sample was very good. The maximum increase in the FWHM of the x-ray beam by a clean fused silica sample was 0.82 arc sec by sample #4, but typically the increase was less than 0.3 arc sec for the other samples.

Carbon particles 10 μm in diameter were deposited on samples #4 and #5. The density of particles on sample #5 was approximately three times the density of those on sample #4. The reflection efficiency of low-density particles was considerably less than for the clean sample and was also less than the high-density particles. It is not clear why the reflection efficiency was higher on the high-density particles, and this area should be studied in more detail. The low-density particles had no significant effect on the scatter curve, but the high-density sample FWHM increased by more than 3 arc sec.

The experimental reflection efficiency measurements and the theoretical calculations on chrominum were in good agreement. Sample #6 was studied at θ values of 0, 20, 40, 85 and 110 arc min to determine the effect of angle of incidence on the scatter curve. There was no significant change in the FWHM on the clean sample. The sample was exposed to a Skylab thermal control material, S13-G paint, for 24 hours. This exposure resulted in a decrease in the reflection efficiency of approximately 20 percent at angles of incidence less than the critical angle. The scatter curve was determined for the contaminated sample at the preceding values of θ and compared to the clean sample. The FWHM of the contaminated curve increased over the clean sample for all values of θ greater than zero and approached an increase of 4 arc sec at θ = 85 arc min.

One sample was allowed to collect dust for 48 hours and then measured. The particle density was 9 particles/mm^2. This contamination resulted in a slightly reduced reflection efficiency and an increase in the FWHM of 0.71 arc sec.

Two samples were contaminated with basalt particles 14 μm in diameter. Sample #8 contained a particle density of 235 particles/mm^2, and sample #9 contained a density several times higher. The reflection efficiency of sample #8 was reduced to a peak value of 60 percent and the scatter curve increased by 3.5 arc sec. The efficiency of sample #9 was very low, with a high value of 11 percent. The scatter curve could not be measured due to the low efficiency.

In summary, the measurements reported in this report confirm (1) that a computer program has been developed to predict the efficiency of optical flats which have a surface finish of at least $\lambda/10$, (2) that particulate matter on the reflecting surface affects the scatter and reflection properties of the sample, and (3) that this effect is a function of composition, particle shape, and density. Also, the study shows that outgassing products deposited on surfaces will reduce the efficiency of an optical surface and will increase the scatter of the x-ray beam by that surface.

REFERENCES

1. Fields, S. A. and Reynolds, J. M.: Device and Method for Determining X-Ray Reflection Efficiency of Optical Surfaces. U.S. Pat. no. 3,702,933, Nov. 14, 1972.

2. Neal, W. R. and Reidy, W. P.: Study on the Effect of Contamination on the Performance of X-Ray Telescopes. Visidyne Inc. Report No. VI-199, Sept. 24, 1973.

3. Hilderbrand, F. B.: Introduction to Numerical Analysis. McGraw-Hill, 1956.

4. Arden, B. W. and Astill, K. N.: "Numerical Algorithms: Origins and Applications." Addison and Wesley, 1970.

5. Trenkle, J. J. and Wilkes, D. R.: Spacecraft Environmental Optical Contamination Problems Associated with Thermal Control Surface Outgassing. ASME 73-ENAs-32, July 16, 1973.

BIBLIOGRAPHY

Alichanow, A. I. and L. A. Arzimowic: Total Reflection of X-Ray by Thin Layers. Zeits. f. Phy., 82, 1933, pp. 489-506.

Cosslett, V.E. and W. C. Nixon: Reflection X-Ray Microscopy: Mirror Systems. Chapter 4 X-Ray Microscopy, Cambridge at the University Press. 1960, pp. 87-122.

Dershem, E.: The Reflection of the K Line of Carbon from Glass. Phy. Rev., Vol. 34, 1929, pp. 1015-1020.

Dershem, E. and M. Schein: The Reflection of the K Line of Carbon from Quartz and Its Relation to Index of Refraction and Absorption Coefficient. Phys. Rev., Vol. 37, May 15, 1931, pp. 1246-1251.

Duncan, R. C. and L G. Parratt: Surface Study of Evaporated Aluminum by X-Ray Total Reflection Method. Bul. Am. Phys. Soc. Vol. 2, 1957, p. 215.

Duncan, R. C. and L. G. Parratt: A Study of Evaporated Aluminum Films by X-Ray Total Reflection. Tech. RPT. No. 13, Dept. of Physics, Cornell University, Ithaca, New York, Aug. 21, 1958.

Elliott, S. B.: Effects of Polishing Imperfections on Specular Reflection of X-Rays. X-ray Optics and X-ray Microanalysis. Edited by H. H. Pattee, V. E. Cosslett and A. Engstrom. Academic Press, 1963.

Ershov, O. A., I. A. Brytov and A. P. Lukirskii: Reflec[illegible] of X-rays from Certain Substances in the Region from 7 to 44 Å. Opt. Sp[illegible]sc., Vol. 22, 1967, pp. 66-69.

Franks, A. and R. F. Braybrook: Analysis of the Lighter Elements by Total Reflection of Their Characteristic X-Ray Wavelengths. Brit. J. Appl. Phys., Vol. 10, pp. 190-192.

Guentert, O. J.: Angular Distribution of Specularly Reflected X-Rays from Thin Films. Phys. Rev., Vol. 138, May 3, 1965, pp. 732-736.

Henderson, J. E. and E. R. Laird: Reflection of Soft X-Rays. Proc. Nat. Acad. Sci., Vol. 14, 1928, pp. 773-777.

BIBLIOGRAPHY (Continued)

Hendrick, R. W., Jr.: Spectral Reflectance of Solids for Aluminum K-Radiation. A dissertation submitted to Stanford University, Stanford, California, 1955.

Hendrick, R. W.: Spectral Reflectance of Solids for Aluminum K Radiation. Jour. Opt. Soc. Am., Vol. 47, Feb. 1957, pp. 165-171.

Johnson, G. L. and R. F. Wuerker: Reflectance Measurements a Carbon-k and Beryllium-k Wavelengths. X-ray Optics and X-ray Microanalysis. Edited by H. H. Pattee, V. E. Cosslett and A. Engstrom, Academic Press, New York, 1963, pp. 229-239.

Lukirskii, A. P. and E. P. Savinov: Reflection of Ultra-Soft X-Radiation from Glass and Titanated Surfaces. Opt. Spectry., Vol. 14, 1963, pp. 152-154.

Lukirskii, A. P., E. P. Savinov, O. A. Ershov and Y. F. Shepelev: Reflection Coefficients of Radiation in the Wavelength Range from 23.6 to 113 Å for a Number of Elements and Substances and the Determination of the Refractive Index and Absorption Coefficient. Opt. Spect., Vol. 16, 1964, pp. 168-172.

Mozzi, R. L. and O. J. Guentert: Adaptation of an X-Ray Diffractometer for Thin Film Studies by Total Reflection of X-Rays. Rev. Sci. Inst., Vol. 35, Jan. 1964, pp. 75-79.

Nigam, A. N.: Origin of Anomalous Surface Reflection of X-rays, Phy. Rev., Vol. 138, May 1965, pp. A1189-A1191.

Parratt, L. G.: Surface Studies of Solids by Total Reflection of X-rays. Phy. Rev., Vol. 95, July 1954, pp. 359-369.

Rieser, L. M., Jr.: Reflection of X-Rays from Condensed Metal Films. Opt. Soc. Am., Vol. 47, Nov. 1957, pp. 987-994.

Sauro, J., I. Fankuchen and N. Wainfan: X-Ray Interference Structure in the Speculary Reflected Radiation from Thin Films. Phy. Rev., Vol. 132, Nov. 1963, pp. 1544-1546.

Schroeder, J. B. and R. G. Klimasewski: Scatter from X-Ray Reflecting Sur ces. The Perkin-Elmer Corporation, Norwalk, Connecticut. Contract NAS -20727, pp. 1-37.

BIBLIOGRAPNY (Concluded)

Schroeder, J. E. and R. G. Klimasewski: Scatter from X-Ray Reflecting Surfaces, Appl. Opt., Vol. 7, October 1968, pp. 1921-1927.

Scott, N. J.: Study of Thin Vacuum Deposited Copper Films by X-Ray Total Reflection. Department of Physics, Cornell University, AFOSR TN-57-779, ASTIA AD-148-010, Tech. Rpt. No. 11, Dec. 1957.

Stewardson, E. A. and J. H. Underwood: The Reflection of Soft X-Rays by Polished Surfaces of Glass and Steel. Brit. J. Appl. Phys., Vol. 16, 1965, pp. 1877-1884.

Wainfan, N., N. J. Scott and L. G. Parratt: Density Measurements of Some Thin Copper Films. Jour. Appl. Phys., Vol. 30, Oct. 1959, pp. 1604-1609.

Wainfan, N. and L. G. Parratt: X-ray Reflection Studies of the Anneal and Oxidation of Some Thin Solid Films. Jour. Appl. Phys., Vol. 31, Aug. 1960, pp. 1331-1337.

Warren, B. E. and J. S. Clarke: Interpretation of the Anomalous Surface Reflection of X-rays. Jour. Appl. Phys., Vol. 36, 1965, pp. 324.

Wuerker, R.: Spectral Reflectance by Solids of Carbon K Radiation: A Dissertation for the Degree of Doctor of Philosophy, Stanford University, March 1960.

Yoneda, Y.: Anomalous Surface Reflection of X-rays. Phy. Rev., Vol. 131, Sept. 1963, pp. 2010-2013.

APPROVAL

X-RAY REFLECTION AND SCATTER MEASUREMENTS ON SELECTED OPTICAL SAMPLES

By Stanley A. Fields, John M. Reynolds, and Robert L. Holland

The information in this report has been reviewed for security classification. Review of any information concerning Department of Defense or Atomic Energy Commission programs has been made by the MSFC Security Classification Officer. This report, in its entirety, has been determined to be unclassified.

This document has also been reviewed and approved for technical accuracy.

William C. Snoddy

WILLIAM C. SNODDY
Chief, Astronomy and Solid State
Physics Division

Charles A. Lundquist

CHARLES A. LUNDQUIST
Director, Space Sciences Laboratory

☆ U S GOVERNMENT PRINTING OFFICE 1976-641-255/241 REGION NO 4